

Galaxy–galaxy lensing by non-spherical haloes – I. Theoretical considerations

Paul J. Howell^{*} and Tereasa G. Brainerd^{*}

Institute for Astrophysical Research, Boston University, 725 Commonwealth Ave., Boston, MA 02215, USA

Accepted 2010 May 7. Received 2010 April 13

ABSTRACT

We use a series of Monte Carlo simulations to investigate the theory of galaxy–galaxy lensing by non-spherical dark matter haloes. The simulations include a careful accounting of the effects of multiple deflections on the galaxy–galaxy lensing signal. In a typical observational data set where the mean tangential shear of sources with redshifts $z_s \simeq 0.6$ is measured with respect to the observed symmetry axes of foreground galaxies with redshifts $z_l \simeq 0.3$, we find that the signature of anisotropic galaxy–galaxy lensing differs substantially from the simple expectation that one would have in the absence of multiple deflections. In general, the observed ratio of the mean tangential shears, $\gamma^+(\theta)/\gamma^-(\theta)$, is strongly suppressed compared to the function that one would measure if the intrinsic symmetry axes of the foreground galaxies were known. Depending upon the characteristic masses of the lenses, the observed ratio of the mean tangential shears may be consistent with an isotropic signal (despite the fact that the lenses are non-spherical), or it may even be reversed from the expected signal (i.e. the mean tangential shear for sources close to the observed minor axes of the lenses may exceed the mean tangential shear for sources close to the observed major axes of the lenses). These effects are caused primarily by the fact that the images of the lens galaxies have, themselves, been lensed and therefore the observed symmetry axes of the lens galaxies differ from their intrinsic symmetry axes. We show that the effects of lensing of the foreground galaxies on the observed function $\gamma^+(\theta)/\gamma^-(\theta)$ cannot be eliminated simply by the rejection of foreground galaxies with very small image ellipticities nor by simply focusing the analysis on sources that are located very close to the observed symmetry axes of the foreground galaxies. We conclude that any attempt to use a measurement of $\gamma^+(\theta)/\gamma^-(\theta)$ to constrain the shapes of dark matter galaxy haloes must include Monte Carlo simulations that take multiple deflections properly into account.

Key words: gravitational lensing – galaxies: haloes – dark matter.

1 INTRODUCTION

Galaxy–galaxy lensing is a form of weak gravitational lensing in which background galaxies are systematically lensed by foreground galaxies. Brainerd, Blandford & Smail (1996, hereafter BBS) published the first statistically significant (4σ) detection of this effect using a small data set that consisted of 439 foreground galaxies, 506 background galaxies and 3202 foreground–background galaxy pairs. Since this early work, galaxy–galaxy lensing has been detected with high precision using various data sets, most of which contain millions of foreground–background galaxy pairs. These high-precision detections have allowed direct constraints to be placed on the nature of the dark matter haloes that surround

the lens galaxies as well as on the bias between mass and light in the universe (see e.g. Fischer et al. 2000; Guzik & Seljak 2002; Hoekstra, Yee & Gladders 2004; Sheldon et al. 2004; Hoekstra et al. 2005; Heymans et al. 2006; Kleinheinrich et al. 2006; Mandelbaum et al. 2006a; Limousin et al. 2007; Parker et al. 2007; Mandelbaum, Seljak & Hirata 2008; Natarajan et al. 2009; Tian, Hoekstra & Zhao 2009).

Observations of galaxy–galaxy lensing by field galaxies have shown that (1) at fixed luminosity, the haloes of red (early-type) galaxies are more massive by a factor of ~ 2 than the haloes of blue (late-type) galaxies (e.g. Guzik & Seljak 2002; Sheldon et al. 2004; Kleinheinrich et al. 2006; Mandelbaum et al. 2006a), (2) the haloes of high-luminosity galaxies are more massive than the haloes of low-luminosity galaxies (e.g. Sheldon et al. 2004; Mandelbaum et al. 2006a) and (3) the dark matter profiles of the haloes are consistent with the spherically averaged Navarro, Frenk & White (NFW)

^{*}E-mail: phowell@bu.edu (PJH); brainerd@bu.edu (TGB)

profile (Navarro, Frenk & White 1995, 1996, 1997; e.g. Hoekstra et al. 2004, 2005; Heymans et al. 2006; Kleinheinrich et al. 2006; Mandelbaum et al. 2008). In other words, observations of galaxy–galaxy lensing by field galaxies have yielded a picture of luminous galaxies and their dark matter haloes that is broadly consistent with the expectations of galaxy formation in the context of the cold dark matter (CDM) model.

Despite the popularity of the spherically averaged NFW density profile, CDM haloes are not spherical. Rather, CDM haloes are triaxial and the degree of flattening increases with halo viral mass (e.g. Warren et al. 1992; Jing & Suto 2002; Bailin & Steinmetz 2005; Kasun & Evrard 2005; Allgood et al. 2006). In principle, galaxy–galaxy lensing should be able to provide constraints on the shapes of the dark matter haloes of field galaxies, since a non-spherical weak lens will produce an anisotropic shear pattern. Consider an isolated weak galaxy lens with a non-spherical dark matter halo (i.e. a halo that, in projection on the sky, has an elliptical surface mass density). For fixed source redshift and fixed angular distance from the lens, sources that are located closer to the major axis of the lens will experience greater shear than sources that are located closer to the minor axis of the lens. If the halo of the lens can be approximated as a singular isothermal ellipsoid with projected ellipticity $\epsilon_{\text{halo}} = 0.3$, the shear experienced by sources nearest the minor axis of the lens will be ~ 80 per cent that of the shear experienced by sources nearest the major axis of the lens (see e.g. Brainerd & Blandford 2002). Although small, such an anisotropy in the galaxy–galaxy lensing signal should be observable provided that, in projection on the sky, mass and light are reasonably well aligned within the lens galaxies.

Weak lensing by galaxy clusters in the Sloan Digital Sky Survey (SDSS; e.g. Abazajian et al. 2009, and references therein) has shown that the dark mass associated with galaxy clusters is non-spherical and has a projected axial ratio of $b/a = 0.48^{+0.14}_{-0.09}$ (Evans & Bridle 2009). The detection of non-spherical haloes by galaxy–galaxy lensing has, however, proven to be more problematical. In a study of galaxy–galaxy lensing by galaxies in the Red-Sequence Cluster Survey, Hoekstra et al. (2004) modelled the projected shapes of the haloes as $\epsilon_{\text{halo}} = \lambda \epsilon_{\text{light}}$, where ϵ_{light} is the ellipticity of the image of the luminous galaxy within the halo. Here $\lambda = 1$ indicates that the projected shapes of the haloes are identical to the shapes of the galaxy images and $\lambda = 0$ indicates that the haloes are perfectly circular in projection on the sky. From their analysis, Hoekstra et al. (2004) concluded that the haloes of their galaxies were somewhat rounder than the images of the galaxies: $\lambda = 0.77^{+0.18}_{-0.21}$. Using the same parametrization of the relationship between the ellipticities of the haloes and the images of the galaxies, Mandelbaum et al. (2006b) found $\lambda = 0.1 \pm 0.06$ for red SDSS lens galaxies and $\lambda = -0.8 \pm 0.4$ for blue SDSS lens galaxies. Here the negative sign indicates an apparent anti-alignment of mass and light for blue SDSS lens galaxies. Finally, Parker et al. (2007) computed the galaxy–galaxy lensing signal using data from the Canada–France–Hawaii Telescope Legacy Survey. When Parker et al. (2007) averaged the signal over all lens galaxies, they found a weak (2σ) preference for the haloes of the lens galaxies to be non-spherical with a projected ellipticity of ~ 0.3 . When Parker et al. (2007) restricted their analysis to elliptical galaxies, the mean halo ellipticity and the significance of the result were found to increase somewhat.

Here we construct a series of Monte Carlo simulations in order to explore the theory of weak galaxy–galaxy lensing by non-spherical dark matter haloes. Using these simulations we demonstrate that, in practice, it is challenging to *interpret* the results of an observational effort to detect anisotropic galaxy–galaxy lensing. This is because,

in general, the observed signature of anisotropic galaxy–galaxy lensing is strongly affected by the fact that the central, ‘lens’ galaxies have themselves been weakly lensed. As a result, the observed symmetry axes of the central, lens galaxies differ from their intrinsic symmetry axes. In our work below, we pay particular attention to the effects of multiple weak deflections on the galaxy–galaxy lensing signal. As was first pointed out by BBS, galaxy–galaxy lensing is inherently a multiple deflection problem. That is, it is common for a source galaxy located at redshift z_s to be weakly lensed by a galaxy located at $z_{l1} < z_s$. Oftentimes, these two galaxies are then subsequently lensed by another galaxy at redshift $z_{l2} < z_{l1}$. In other words, the galaxy at z_{l1} serves simultaneously as a lens for the galaxy at z_s and a source for the galaxy at z_{l2} . In addition, the galaxy at z_s is lensed by two different foreground galaxies. Neglecting such multiple deflections when modelling an observed galaxy–galaxy lensing signal will give rise to incorrect conclusions about the underlying properties of the haloes of the lens galaxies. For a detailed discussion of the frequency and relative strengths of multiple deflections in a deep galaxy–galaxy lensing data set, the reader is referred to Brainerd (2010).

Below, the haloes of the lens galaxies will be modelled as truncated singular isothermal ellipsoids. This choice is motivated by two considerations. First, the singular isothermal ellipsoid gives rise to a gravitational lensing shear that can be computed analytically (e.g. Kormann, Schneider & Bartelmann 1994). Secondly, at the present time the observational galaxy–galaxy lensing data are not of sufficiently high quality to allow one to distinguish between singular isothermal ellipsoid haloes and those that are triaxial CDM haloes.

The outline of the paper is as follows. In Section 2, we present the basic theory of gravitational lensing by singular isothermal ellipsoids and introduce a shorthand notation that we will use throughout the paper. In Section 3, we outline the construction of Monte Carlo simulations of galaxy–galaxy lensing by non-spherical haloes, where the locations and apparent magnitudes of the Monte Carlo galaxies are taken from a large observational data set. In Section 4, we present the signature of galaxy–galaxy lensing by non-spherical haloes that one should expect to obtain from a realistic observational data set. In Section 5, we explore the effects of galaxy–galaxy lensing on the images of relatively nearby galaxies (i.e. galaxies that are ordinarily considered to be ‘lenses’ but are not always considered to be ‘sources’). In Section 6, we construct a second suite of Monte Carlo simulations in order to determine the effect of multiple weak deflections on observations of anisotropic galaxy–galaxy lensing. In Section 7, we demonstrate that the effects of lensing of foreground galaxies on the observed signature of anisotropic galaxy–galaxy lensing cannot be eliminated by selective rejection of either lens or source galaxies. We summarize our results and present our conclusions in Section 8. Throughout, we will refer to the weak lensing of a background galaxy by a single foreground galaxy as a ‘deflection’, and we will adopt a flat Λ -dominated cosmology with $H_0 = 70 \text{ km s}^{-1} \text{ Mpc}^{-1}$, $\Omega_{m0} = 0.3$ and $\Omega_{\Lambda0} = 0.7$.

2 TRUNCATED SINGULAR ISOTHERMAL ELLIPSOID LENSES

Let us assume that the dark matter haloes of large, luminous galaxies may be fairly represented as truncated singular isothermal ellipsoids. Since we are only concerned with the weak lensing regime, the adoption of a halo model that is singular (as opposed to a model with a finite density core) will have no effect on our results below.

Following Kormann et al. (1994), the surface mass densities of the dark matter haloes are given by

$$\Sigma(\rho) = \frac{\sigma_v^2 \sqrt{f}}{2G} \left(\frac{1}{\rho} - \frac{1}{\sqrt{\rho^2 + x_t^2}} \right), \quad (1)$$

where σ_v is the line-of-sight velocity dispersion, f is the axial ratio of the mass distribution as projected on the sky ($0 < f \leq 1$), x_t is the truncation radius, G is Newton's constant and ρ is a generalized elliptical radius defined such that $\rho^2 = x_1^2 + f^2 x_2^2$. Here x_1 and x_2 are Cartesian coordinates measured, respectively, along the minor and major axes of the projected mass distribution of the halo. In the limiting case of a round lens (i.e. $f \rightarrow 1$), the total mass of the halo becomes

$$M_{\text{tot}} = \frac{\pi \sigma_v^2 x_t}{G}. \quad (2)$$

The convergence (κ) and shear ($\gamma \equiv \gamma_1 + i\gamma_2$) are the characteristic properties of a gravitational lens. In the case of truncated singular isothermal ellipsoid lenses, the convergence is given by

$$\kappa(\rho) = \frac{\sigma_v^2 \sqrt{f}}{2G \Sigma_c} \left(\frac{1}{\rho} - \frac{1}{\sqrt{\rho^2 + x_t^2}} \right), \quad (3)$$

where $\Sigma_c \equiv \left(\frac{4\pi G}{c^2} \frac{D_l D_s}{D_s} \right)^{-1}$ is the critical surface mass density, D_l is the angular diameter distance of the lens, D_s is the angular diameter distance of the source and D_{ls} is the angular diameter distance between the lens and the source. The real and imaginary components of the shear can be obtained straightforwardly from equations (63abc) of Kormann et al. (1994):

$$\gamma_1 = \frac{\sigma_v^2 \sqrt{f}}{2G \Sigma_c} \left[-\frac{\cos(2\varphi)}{\rho} - \{f^2(x_1^2 - x_2^2) - (1 - f^2)x_t^2\} \mathcal{P} \right] \quad (4)$$

$$\gamma_2 = \frac{\sigma_v^2 \sqrt{f}}{2G \Sigma_c} \left[-\frac{\sin(2\varphi)}{\rho} - 2f^2 x_1 x_2 \mathcal{P} \right], \quad (5)$$

where

$$\mathcal{P} \equiv \frac{x_1^2 + f^4 x_2^2 - (1 + f^2)(\rho^2 + x_t^2) + 2f x_t \sqrt{\rho^2 + x_t^2}}{\sqrt{\rho^2 + x_t^2} [f^4 r^4 - 2f^2(1 - f^2)x_t^2(x_1^2 - x_2^2) + (1 - f^2)x_t^4]} \quad (6)$$

(e.g. Wright 2002). Again, x_1 and x_2 are Cartesian coordinates measured along the minor and major axes of the lens, respectively. In order to maintain consistency with the notation of Kormann et al. (1994), here we have used a polar coordinate system, centred on the lens, with radial coordinate $r \equiv \sqrt{x_1^2 + x_2^2}$ and polar angle φ defined such that $x_1 = r \cos \varphi$ and $x_2 = r \sin \varphi$.

It is clear from equations (4)–(6) that, unlike a circularly symmetric lens for which the magnitude of the shear depends upon the angular distance from the lens centre but not the azimuthal coordinate of the source, the shear due to an elliptical lens is a function of both the angular distance from the lens centre and the azimuthal coordinate of the source. At a given angular distance, θ , from the centre of an elliptical lens, the magnitude of the shear is greatest for sources located nearest the major axis of the lens and least for sources located nearest the minor axis of the lens. Hence, within a given radial annulus that is centred on the elliptical lens, sources whose azimuthal coordinates, φ , place them within $\pm 45^\circ$ of the major axis of the lens will experience a greater mean shear than sources whose azimuthal coordinates, φ , place them within $\pm 45^\circ$ of the minor axis of the lens. As a shorthand notation, we will refer to the magnitude of the mean shear experienced by sources whose

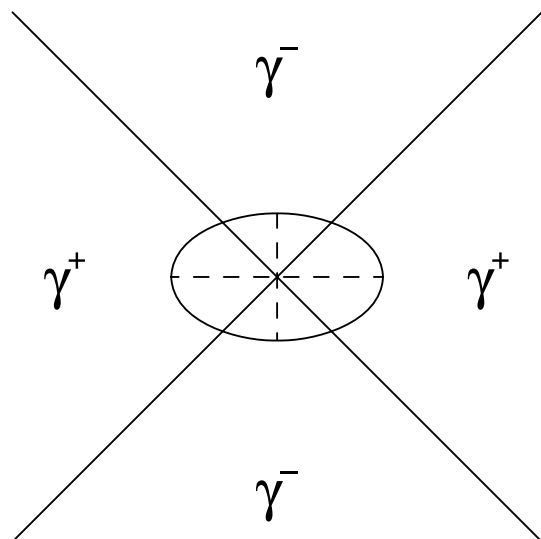


Figure 1. Illustration of our notation, γ^+ and γ^- (see the text).

azimuthal coordinates place them within $\pm 45^\circ$ of the minor axis of an elliptical lens as γ^- . Similarly, we will refer to the magnitude of the mean shear experienced by sources whose azimuthal coordinates place them within $\pm 45^\circ$ of the major axis of an elliptical lens as γ^+ (see Fig. 1).

3 MONTE CARLO SIMULATIONS OF GALAXY–GALAXY LENSING IN THE BTC40 SURVEY

To quantify the effects of non-spherical dark matter haloes on the galaxy–galaxy lensing signal, we construct a series of Monte Carlo simulations. As a starting point for our simulations, we use a set of modestly deep, wide-field *I*-band images that were generously donated to us by Emilio Falco. The images were obtained as part of the BTC40 survey (Monier et al. 2002), which was carried out using the Big Throughput Camera (BTC; Tyson et al. 1992; Wittman et al. 1998) on the 4-m Blanco telescope at the Cerro-Tololo Inter-American Observatory. The *I*-band exposures consist of 150 s per pointing, and each individual image covers an area of the order of one-quarter of a deg^2 . We selected a total of 13.8 deg^2 of imaging data from the survey for our work, rejecting images that were obtained during poor photometric conditions or that exhibited poor tracking or poor focus. The data were calibrated, flat-fielded and de-fringed as described in Monier et al. (2002). Object catalogues were created from the reduced *I*-band data using the SExtractor package (Bertin & Arnouts 1996).

Additional details regarding the quality of the imaging, star–galaxy separation, cosmic ray rejection, point-spread function correction and masking of cosmetic defects (e.g. large stellar blooms, diffraction spikes) will be presented in a companion paper (Howell & Brainerd, in preparation). In the companion paper, we will also present an analysis of the observed galaxy–galaxy lensing signal in this data set. For the purposes of our present study, we are simply interested in using the BTC40 galaxies as the framework for a set of Monte Carlo simulations of galaxy–galaxy lensing by non-spherical haloes. That is, here we will address the following question: given a data set like that obtained from the BTC40, what should one expect to observe for the galaxy–galaxy lensing signal if the dark matter haloes of the galaxies are non-spherical? The information from the BTC40 images that we use here consists solely of

the centroids of the galaxies and their I -band apparent magnitudes. These, along with other quantities, are used as input parameters for our Monte Carlo simulations. Also, in order to ultimately match the data that will be presented in our companion paper, here we use only BTC40 galaxies with $18 \leq I_{AB} \leq 22.5$. While the completeness limit of the data is somewhat fainter than $I_{AB} = 22.5$, in practice the BTC40 galaxies with $I_{AB} > 22.5$ are too small for accurate shape determinations.

The observed shapes of the BTC40 galaxies have been affected by the presence of a spatially varying anisotropic point spread function. Because of this, and because of the fact that shape determinations become increasingly noisy at faint flux levels, we do not use the observed shapes of the BTC40 galaxies in our Monte Carlo simulations. Instead, in order to describe the shape of the luminous galaxy, each Monte Carlo galaxy is assigned an intrinsic image ellipticity, $\epsilon_{in} \equiv (a - b)/(a + b)$, that is drawn from the probability distribution derived by Ebbels (1998) from 94 archival *Hubble Space Telescope* field survey images:

$$P(\tau) = \mathcal{A} \tau \exp[-(\tau/0.036)^{0.54}]. \quad (7)$$

Here $\tau = (a^2 - b^2)/(2ab)$, \mathcal{A} is a normalizing constant and a and b are, respectively, the semimajor and semiminor axes of the intrinsic image ellipses, respectively.

We assume that the projected shapes of the haloes of the BTC40 galaxies are elliptical but, unlike Hoekstra et al. (2004) and Mandelbaum et al. (2006b), we do not assume that there is a linear relationship between the shape of the luminous galaxy and the shape of its projected dark matter halo. While the assumption $\epsilon_{halo} = \lambda \epsilon_{light}$ may have some validity for elliptical galaxies, it is definitely false for disc galaxies (which make up a substantial fraction of the lens population). Agustsson & Brainerd (2006) showed that the observed ellipticities of disc galaxies embedded within CDM haloes were largely uncorrelated with the ellipticities of their projected haloes (see their fig. 6). This is due to the fact that one always views a random projection of the dark matter halo on the sky. Therefore, a high inclination angle for the disc (which maximizes the ellipticity of the luminous galaxy image) does not, in general, correlate with a projection that maximizes the projected ellipticity of the halo. In order to assign projected axial ratios, f , to the haloes of our

Monte Carlo galaxies, we use the probability distribution obtained by Agustsson & Brainerd (2006) for the projected axial ratios of CDM galaxy haloes. The halo of each galaxy in our simulations is therefore assigned a value of f that is drawn at random from this distribution (see Fig. 2).

Next, we must make a choice as to how to orient the luminous galaxies within their dark matter haloes. The only symmetry axes that can be used in an observational data set to detect anisotropic galaxy–galaxy lensing are, of course, the symmetry axes of the luminous galaxies themselves. If mass and light are not reasonably well aligned within the lens galaxies, a detection of anisotropic galaxy–galaxy lensing is hopeless since we cannot directly observe the orientations of the symmetry axes of the dark matter haloes. Therefore, in our simulations we will assume that the intrinsic symmetry axes of the luminous galaxies and their dark matter haloes are aligned with each other. This assumption maximizes the degree of anisotropy in the galaxy–galaxy lensing signal that one should expect to see and it presents a best-case scenario for detecting the effect.

Neither spectroscopic redshifts nor photometric redshifts are available for the BTC40 galaxies. Therefore, we must assign redshifts to the galaxies in order to carry out our Monte Carlo simulations. Following the prescriptions of BBS and Wright (2002), we adopt a redshift distribution of the form

$$P(z|I_{AB}) = \frac{\beta z^2 \exp[-(z/z_0)^\beta]}{\Gamma(3/\beta)z_0^3}. \quad (8)$$

Taking $\beta = 1.5$ yields good agreement with the redshift surveys of LeFèvre et al. (1996), LeFèvre et al. (2004), and we then have

$$z_0 = 0.8 [0.86 + 0.15(I_{AB} - 23.35)]. \quad (9)$$

Finally, we must assign velocity dispersions and truncation radii to the haloes of each of the Monte Carlo galaxies. To do this, we assume that the galaxies follow a Faber–Jackson or Tully–Fisher type of relationship and have a constant mass-to-light ratio (see e.g. BBS). The velocity dispersion, σ_v , of the halo of a galaxy with luminosity, L , is then given by

$$\frac{\sigma_v}{\sigma_v^*} = \left(\frac{L}{L^*} \right)^{1/4}, \quad (10)$$

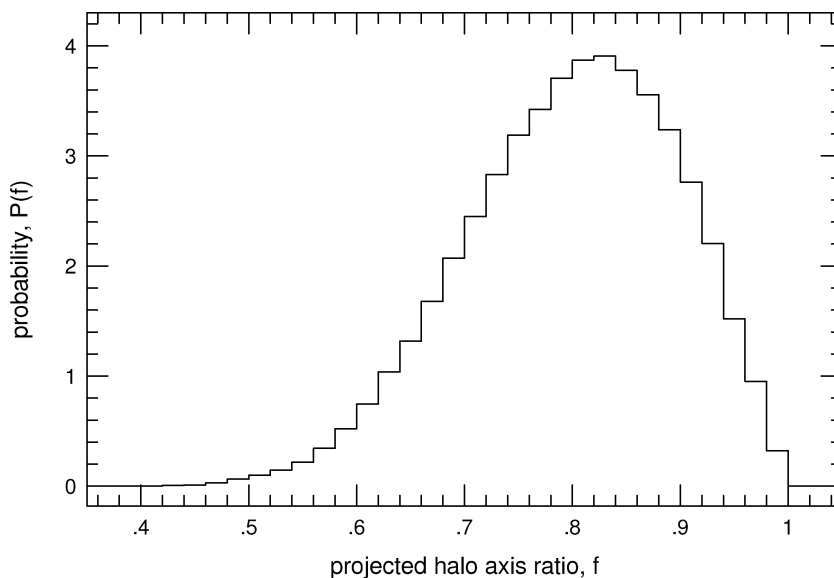


Figure 2. Distribution of projected axial ratios, f , for the Monte Carlo dark matter haloes (following the results of Agustsson & Brainerd 2006).

where σ_v^* is the velocity dispersion of the halo of an L^* galaxy. The truncation radius, x_t , of the halo of a galaxy with luminosity, L , is given by

$$\frac{x_t}{x_t^*} = \left(\frac{L}{L^*} \right)^{1/2}, \quad (11)$$

where x_t^* is the truncation radius of the halo of an L^* galaxy. The luminosity of each Monte Carlo galaxy is obtained from its observed I -band apparent magnitude and the redshift, z , that was assigned to the galaxy based on equation (8). Accounting for the K -correction, we have

$$\frac{L}{L^*} = \left(\frac{H_0 D_l}{c} \right) (1+z)^{1+\alpha} 10^{0.4(22.9-I_{AB})}, \quad (12)$$

where $\alpha = -\frac{d \log_{10} L_v}{dv}$ (e.g. BBS). For simplicity, we take $\alpha = 0.42$, which is the mean slope of the spectral energy distribution between the Johnson R band and B band from the Caltech Faint Galaxy Redshift Survey (Cohen et al. 1999a,b).

For each Monte Carlo simulation then,

- (i) a pair of characteristic parameters, (σ_v^*, x_t^*) , are adopted for the haloes of L^* galaxies;
- (ii) each luminous galaxy is assigned its observed location on the image as well as its observed I -band apparent magnitude;
- (iii) the image of each luminous galaxy is assigned an intrinsic shape, $\epsilon_{in} \equiv (a-b)/(a+b)$, using equation (7) and its dark matter halo is assigned an axial ratio, f , drawn from the projected halo shapes in Agustsson & Brainerd (2006);
- (iv) each luminous galaxy is assigned a random intrinsic position angle, ϕ_{in} (i.e. we assume that in the absence of gravitational lensing, the galaxy images are uncorrelated), and, since we also assume that mass and light are aligned in projection on the sky, the projected halo is assigned a position angle identical to the position angle of the unlensed luminous galaxy;
- (v) each galaxy is assigned a redshift, z , using equation (8), and its luminosity relative to L^* is obtained using equation (12);
- (vi) the dark matter halo of each galaxy is assigned a velocity dispersion, σ_v , and truncation radius, x_t , based upon the luminosity of the galaxy within the halo and the scaling relations of equations (10) and (11).

Each Monte Carlo simulation then proceeds by computing the weak lensing shear, γ , that is induced as light rays emanating from distant galaxies encounter the gravitational potentials of foreground galaxies. As we will see below, most of the distant galaxies with redshift z_i are lensed by numerous foreground galaxies with redshifts $z_j < z_i$. We define the intrinsic (unlensed) shape of each luminous Monte Carlo galaxy to be

$$\chi_{in} = \epsilon_{in} e^{2i\phi_{in}}, \quad (13)$$

where ϵ_{in} is the intrinsic (unlensed) ellipticity of the galaxy image and ϕ_{in} is the intrinsic (unlensed) position angle. Since we are dealing with the weak lensing regime, all lensing events may be considered to be independent (e.g. Bartelmann & Schneider 2001) and the final image shape of each lensed galaxy is given by

$$\chi_f = \chi_{in} + \sum_{j=1}^{N_{lens}} \gamma_j = \chi_{in} + \chi_{net}, \quad (14)$$

where γ_j is the shear induced by foreground lens galaxy, j , and χ_{net} is the net shear due to all foreground lenses. The real (γ_1) and imaginary (γ_2) components of the shear are given by equations (4)–(6).

Computation of the net shear for each of the galaxies due to literally *all* potential foreground lens galaxies is extremely time

consuming and, from a practical standpoint, is unnecessary since foreground lenses that induce negligible shear (say, $\gamma_j \sim 10^{-9}$) can be neglected in comparison to foreground lenses that induce substantial shear (say, $\gamma_j > 0.005$). From Brainerd (2010), we know that source galaxies with a median redshift $z_s = 0.96$ that have been lensed by a population of foreground galaxies with $z_l = 0.55$ experience little shear due to lenses that are located at projected radii $\theta > 60$ arcsec. Scaling to the BTC40 galaxies, we find that for $\theta > 100$ arcsec the contribution to the net galaxy–galaxy lensing shear will be negligible. Hence, in our Monte Carlo simulations we compute the net shear experienced by each BTC40 galaxy due to all foreground galaxies that are located within a projected radius of 100 arcsec, and we do not include any contribution to the net shear from lenses located at projected radii of > 100 arcsec.

In the next section, we will analyse the output of our Monte Carlo simulations in a manner that is similar to the way in which an observational galaxy–galaxy lensing data set is analysed. In the case that neither spectroscopic nor photometric redshifts are available for an observational data set (as is the case for the BTC40 data), one can make only a crude distinction between ‘foreground’ and ‘background’ galaxies using apparent magnitudes. From the probability distribution above, we know that, on average, galaxies with bright apparent magnitudes tend to be located at lower redshifts than galaxies with faint apparent magnitudes (though there is certainly a good deal of overlap). If we consider galaxies with $18 \leq I_{AB} \leq 20$, we find a median redshift of $z_{med} = 0.29$ for our BTC40 sample. If we consider galaxies with $20 < I_{AB} \leq 22.5$, we find a median redshift of $z_{med} = 0.61$ for our BTC40 sample. These magnitude cuts therefore yield a rough division of our BTC40 sample into 38 879 ‘bright’ foreground ($18 \leq I_{AB} \leq 20$) objects and 225 518 ‘faint’ background ($20 < I_{AB} \leq 22.5$) objects. The redshift distributions adopted for these objects are shown in Fig. 3.

It is important to remember that in the Monte Carlo simulations, all galaxies with redshifts z_i have been lensed by all other galaxies with redshifts $z_j < z_i$ that are located within a projected radius $\theta = 100$ arcsec of the galaxy at redshift z_i . We illustrate this in Fig. 4, where we show an example of a Monte Carlo simulation. The image corresponds to a single CCD frame from the BTC40 survey ($0'.25 \times 0'.25$), where the dots indicate the locations of galaxies with magnitudes $18 \leq I_{AB} \leq 22.5$ and the lines indicate the directions on the sky of objects that have lensed the galaxies. That is, each line indicates the presence of a lens–source pair in the data; however, for clarity of the figure we do not extend the lines to connect every source galaxy directly to all of its lenses. Brown dots show the locations of bright, foreground galaxies ($18 \leq I_{AB} \leq 20$) and blue dots show the locations of faint, background galaxies ($20 < I_{AB} \leq 22.5$). Blue lines indicate that the lens is a faint, background galaxy. Brown lines indicate that the lens is a bright, foreground galaxy. Therefore, a blue line originating from a blue dot indicates that a faint, background galaxy has been lensed by another faint, background galaxy. Similarly, a brown line originating from a blue dot indicates that a faint, background galaxy has been lensed by a bright, foreground galaxy. Importantly, Fig. 4 shows that virtually all of the bright, foreground galaxies (the brown dots) have, themselves, been lensed multiple times. Most of the bright, foreground galaxies have been lensed by other bright galaxies, but they are occasionally lensed by a faint galaxy (due to the overlapping redshift distributions of these objects). The majority of the lenses turn out to be faint galaxies simply because there are approximately six times as many faint galaxies per unit area as there are bright galaxies.

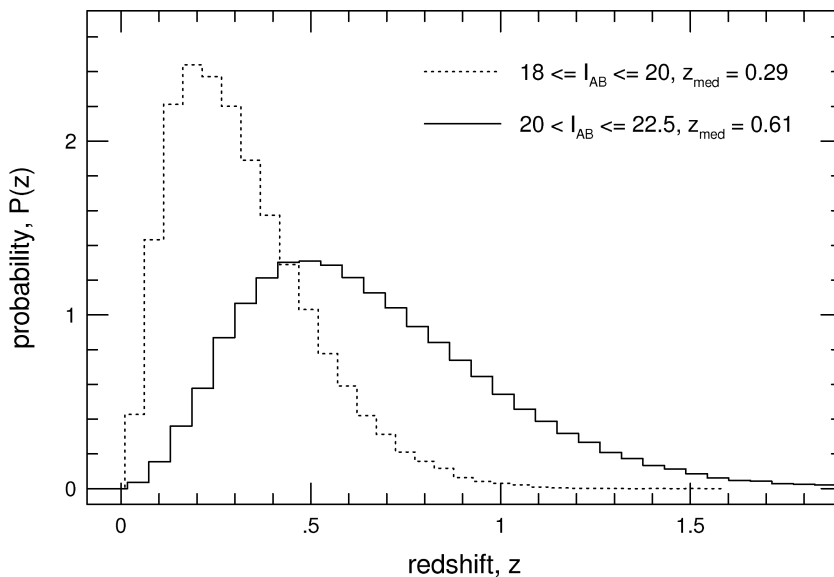


Figure 3. Redshift distributions adopted for the ‘bright’ foreground ($18 \leq I_{AB} \leq 20$) and ‘faint’ background ($20 < I_{AB} \leq 22.5$) galaxies in the BTC40 sample.

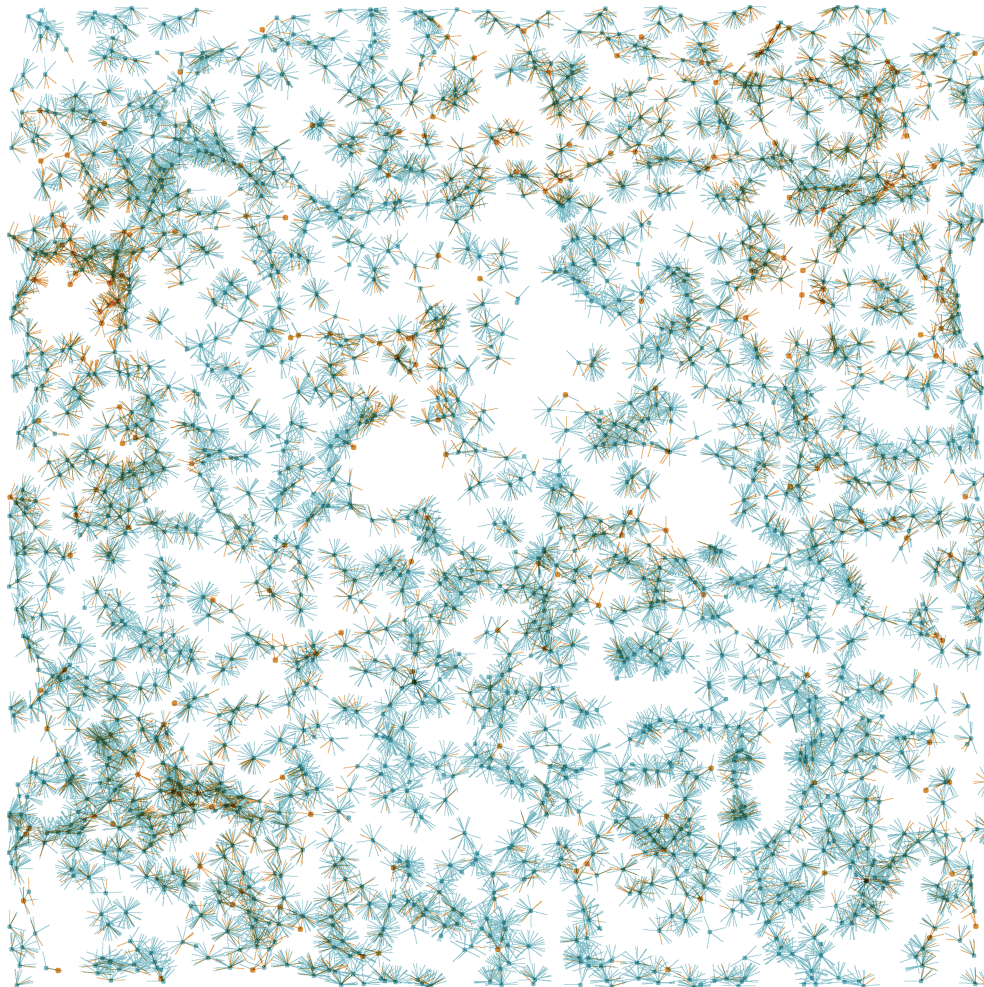


Figure 4. Results of one Monte Carlo simulation for one CCD frame from the BTC40 data. Brown dots show the locations of bright, foreground galaxies ($18 \leq I_{AB} \leq 20$) and blue dots show the locations of faint, background galaxies ($20 < I_{AB} \leq 22.5$). Lines indicate the direction on the sky of objects that have lensed a given galaxy. Blue lines indicate that the lens is a faint galaxy; brown lines indicate that the lens is a bright galaxy. Note that virtually all bright, foreground galaxies have been lensed multiple times.

It is clear from Fig. 4 that the vast majority of the galaxies have been lensed by more than one galaxy; that is, multiple deflections are common for all of the galaxies in the Monte Carlo simulations. This statement is true independent of the values of the characteristic parameters adopted for the haloes of L^* galaxies, (σ_v^*, x_t^*) ; however, the relative strengths of the individual deflections and their net effect on χ_f for each galaxy will, of course, be a strong function of the values of the characteristic parameters that are adopted (see e.g. Brainerd 2010).

4 SIGNATURE OF ANISOTROPIC GALAXY–GALAXY LENSING

Here we use the output of the BTC40 Monte Carlo simulations to compute the dependence of the mean tangential shear of the faint ($20 < I_{AB} \leq 22.5$) galaxies using the bright ($18 \leq I_{AB} \leq 20$)

galaxies as the centres for the calculation. That is, we compute the signature of galaxy–galaxy lensing in the same way as is done for an observational data set in which apparent magnitude is used as the sole discriminator between ‘foreground’ and ‘background’ objects. We separately compute $\gamma^+(\theta)$ and $\gamma^-(\theta)$, and we show the results in Figs 5–7 for three different sets of characteristic parameters that were chosen to represent the haloes of L^* galaxies. Since galaxy–galaxy lensing is relatively insensitive to the radii of the dark matter haloes (e.g. BBS; Hoekstra et al. 2004; Brainerd 2010), we adopt a value of $x_t^* = 100 h^{-1}$ kpc for the haloes of L^* galaxies. In Figs 5–7 we then vary the characteristic velocity dispersion, adopting values of $\sigma_v^* = 100 \text{ km s}^{-1}$ (Fig. 5), $\sigma_v^* = 150 \text{ km s}^{-1}$ (Fig. 6) and $\sigma_v^* = 200 \text{ km s}^{-1}$ (Fig. 7).

In order to compute $\gamma^+(\theta)$ and $\gamma^-(\theta)$, we must first define what we mean by the symmetry axes of the bright galaxies. Implicit in our definition of γ^+ and γ^- is that the intrinsic (unlensed)

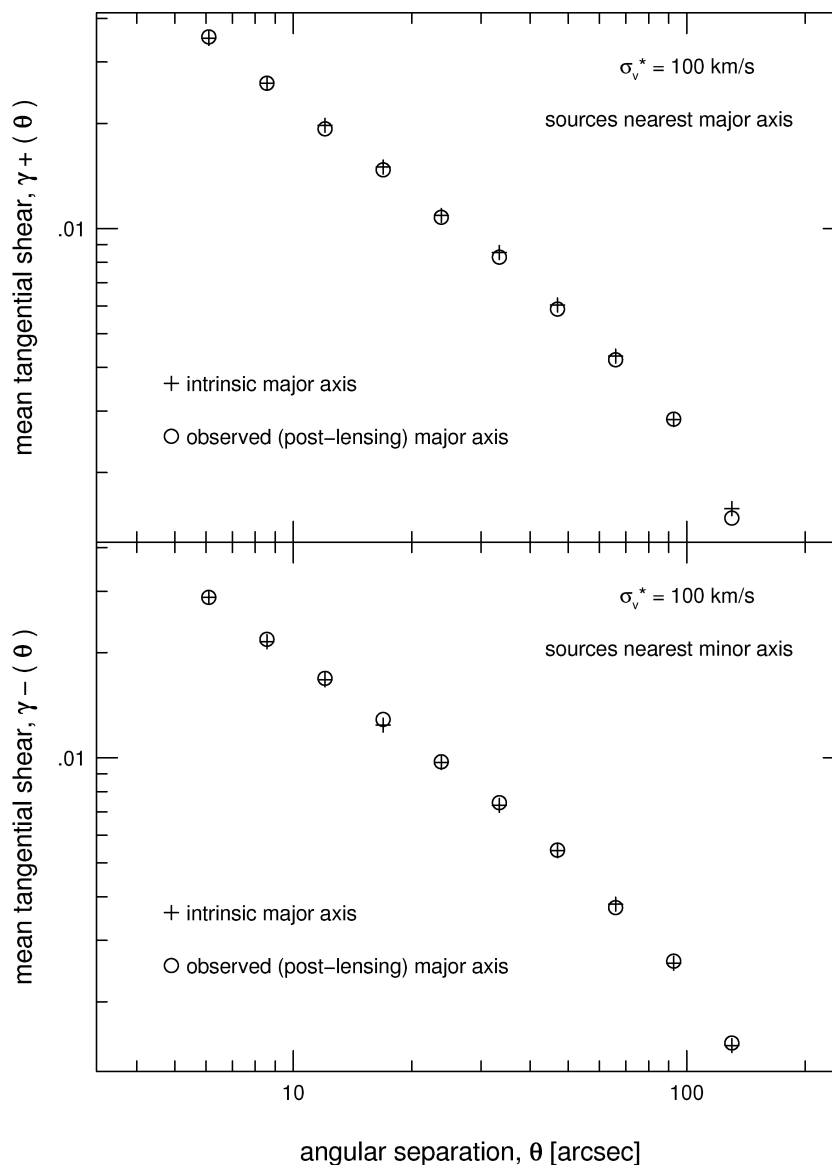


Figure 5. Observed functions, $\gamma^+(\theta)$ and $\gamma^-(\theta)$, from the BTC40 Monte Carlo simulations. Results show the mean of 15 independent realizations of the complete BTC40 data set. All source galaxies that are located within $\pm 45^\circ$ of the symmetry axes of the bright, foreground centres are used in the calculations. Different point types indicate different definitions of the symmetry axes of the bright, foreground centres (circles: observed symmetry axes after lensing, crosses: intrinsic symmetry axes). Error bars are omitted because they are smaller than the data points. Here the characteristic parameters for the haloes of L^* galaxies are $\sigma_v^* = 100 \text{ km s}^{-1}$ and $x_t^* = 100 h^{-1}$ kpc.

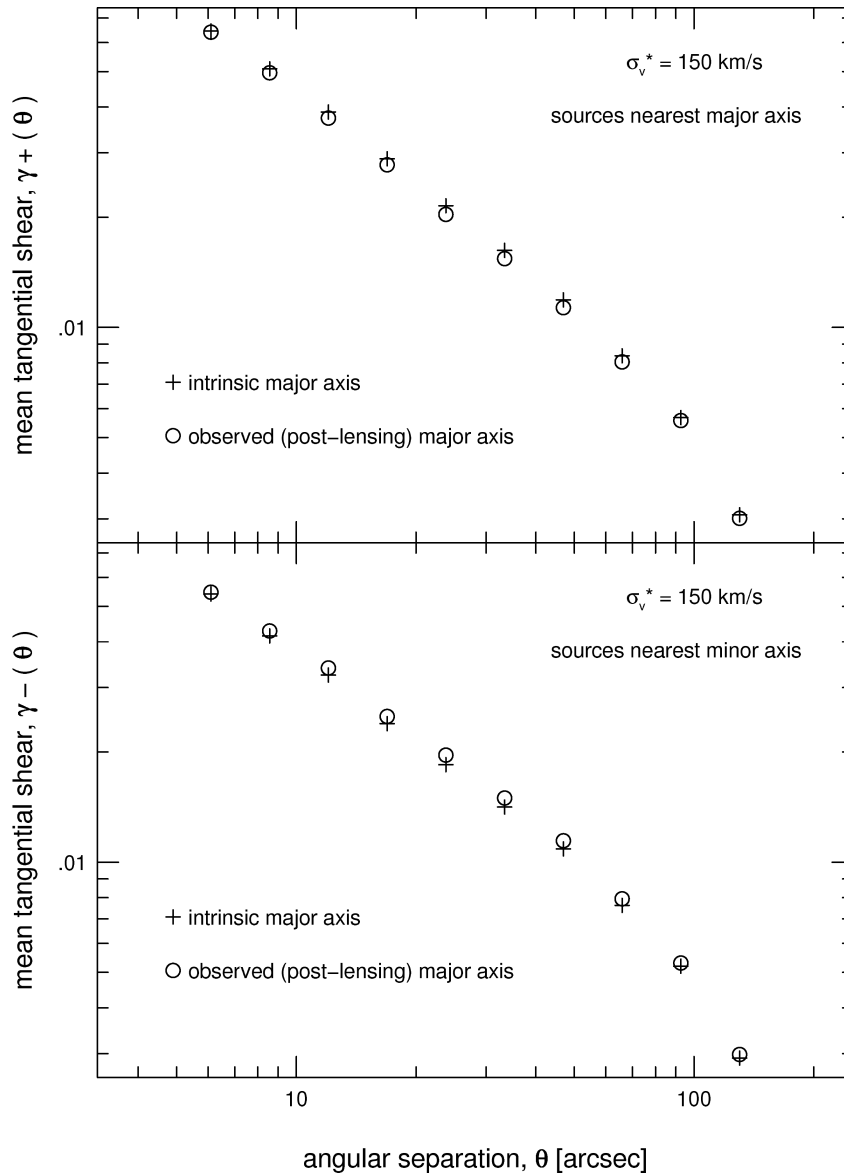


Figure 6. Same as Fig. 5, except that here $\sigma_v^* = 150 \text{ km s}^{-1}$.

symmetry axes are the symmetry axes of the projected dark matter halo (e.g. Fig. 1). However, observers are not blessed with ‘dark matter glasses’ that allow us to see the intrinsic symmetry axes. Rather, in an observational data set, we must take the symmetry axes of the bright galaxies to be their *observed* symmetry axes, not their intrinsic symmetry axes. This is an important distinction since the observed symmetry axes of the bright galaxies may have been altered due to weak lensing by foreground galaxies (see e.g. Fig. 4).

In Figs 5–7 we compute $\gamma^+(\theta)$ and $\gamma^-(\theta)$ using both the observed symmetry axes (circles) and the intrinsic symmetry axes (crosses) of the bright, central galaxies. That is, the circles indicate the functions that we would expect to measure in an observational data set, while the crosses indicate the functions that we would obtain if we were able to observe the intrinsic (unlensed) symmetry axes of the bright, central galaxies. In the case of very low-mass lenses (Fig. 5), there is relatively little difference between the tangential shears that result from using the observed symmetry axes of the bright centres and those that result from using the intrinsic symmetry axes. However, for moderate to high-mass lenses (Figs 6 and 7), it is

clear that over most scales there is a systematic difference between the two calculations. In particular, over most scales the observed values of $\gamma^+(\theta)$ in Figs 6 and 7 are systematically lower than the values that are obtained by using the intrinsic symmetry axes of the bright centres. Conversely, over most scales the observed values of $\gamma^-(\theta)$ in Figs 6 and 7 are systematically higher than the values that are obtained by using the intrinsic symmetry axes of the bright centres.

Shown in Fig. 8 is the ratio of the mean tangential shears, $\gamma^+(\theta)/\gamma^-(\theta)$, for our three halo models. From this figure, we see that for low-mass haloes ($\sigma_v^* = 100 \text{ km s}^{-1}$) the ratio of the mean tangential shears is slightly lower on average when the shear is measured with respect to the observed symmetry axes of the bright centres than when it is measured with respect to the intrinsic symmetry axes. However, to within the error bars, the two functions formally agree. For moderate ($\sigma_v^* = 150 \text{ km s}^{-1}$) to high ($\sigma_v^* = 200 \text{ km s}^{-1}$) mass lenses, there is a substantial suppression of $\gamma^+(\theta)/\gamma^-(\theta)$ when the observed symmetry axes of the bright centres are used compared to what one would obtain using the intrinsic symmetry axes. In the

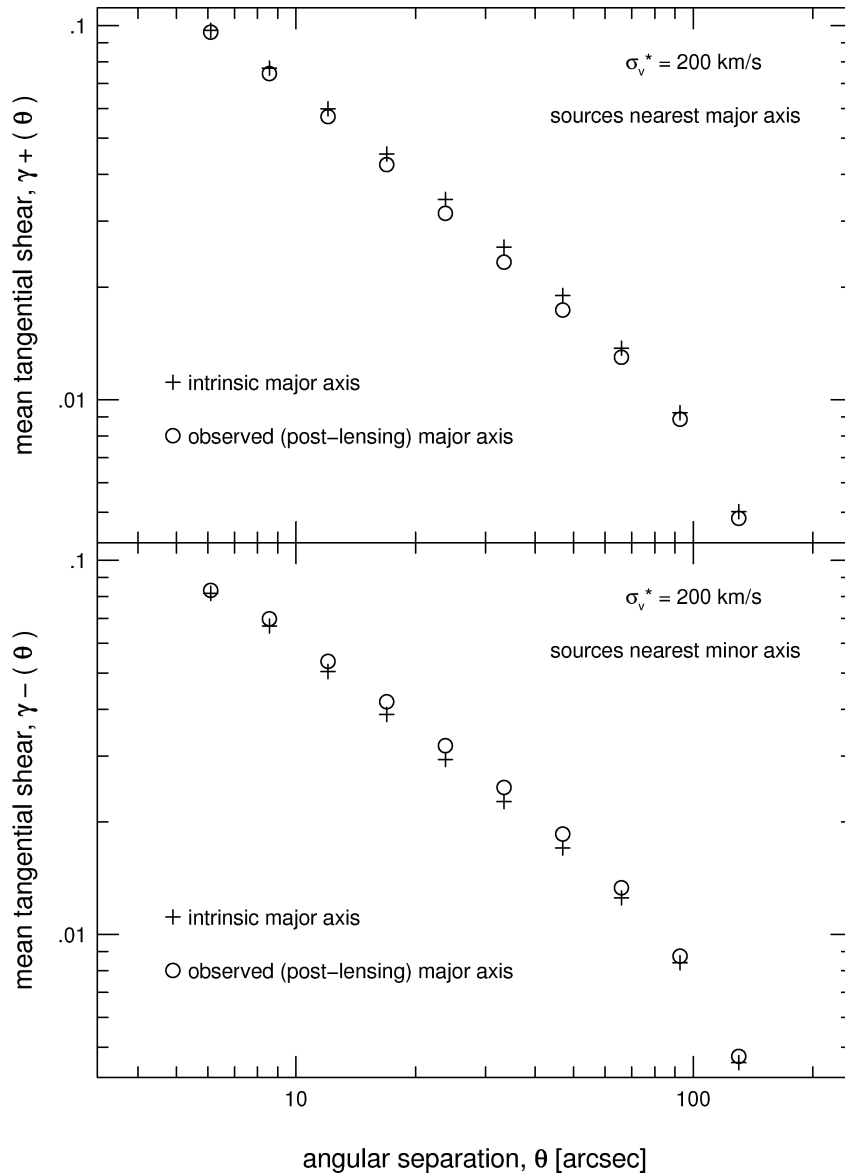


Figure 7. Same as Fig. 5, except that here $\sigma_v^* = 200 \text{ km s}^{-1}$.

case of $\sigma_v^* = 150 \text{ km s}^{-1}$, there is little to no anisotropy apparent on scales $\theta > 20$ arcsec. That is, the observed signature of anisotropic galaxy–galaxy lensing by haloes of moderate mass is largely consistent with isotropic galaxy–galaxy lensing on scales $\theta > 20$ arcsec. In the case of $\sigma_v^* = 200 \text{ km s}^{-1}$, the observed function is actually *reversed* from the expected function [i.e. $\gamma^+(\theta) < \gamma^-(\theta)$] on scales $20 \text{ arcsec} < \theta < 70 \text{ arcsec}$. That is, the observed signature of anisotropic galaxy–galaxy lensing by high-mass haloes could lead one to think (falsely) that mass and light are anti-aligned within the galaxies.

Fig. 8 demonstrates, then, that an observation of $\gamma^+(\theta) = \gamma^-(\theta)$ is *not* categorical proof that the haloes of the lenses are spherically symmetric since the haloes of our Monte Carlo galaxies are non-spherical. In addition, an observation of $\gamma^+(\theta) < \gamma^-(\theta)$ is *not* categorical proof that mass and light are anti-aligned within the lens galaxies since the intrinsic symmetry axes of the luminous galaxies in the Monte Carlo simulations were taken to be aligned with the symmetry axes of their projected dark matter haloes. Since we have allowed the bright, central galaxies that we have used to

compute $\gamma^+(\theta)$ and $\gamma^-(\theta)$ to be lensed by foreground galaxies, the circles in Fig. 8 show the actual signature of galaxy–galaxy lensing by non-spherical dark matter haloes that one should expect to see in an observational data set (i.e. a data set in which the galaxies are all broadly distributed in redshift space). Contrary to the usual expectation that $\gamma^+(\theta)$ should exceed $\gamma^-(\theta)$ over a wide range of angular scales, Fig. 8 shows that this is unlikely to be the case unless the haloes of L^* galaxies have particularly low characteristic velocity dispersions ($\sigma_v^* = 100 \text{ km s}^{-1}$). In Section 6, we will demonstrate that the results shown in Fig. 8 are caused primarily by the fact that the observed symmetry axes of the bright, foreground centres have been altered from their intrinsic symmetry axes by weak lensing.

Figs 9 and 10 show schematic illustrations of what can occur in a situation where a given lens–source pair is, itself, lensed by a foreground mass. Consider an intrinsically circular source galaxy that is located near the major axis of an elliptical lens galaxy. That is, the lens–source pair is in what one might call the ‘ γ^+ configuration’. After being sheared by the elliptical lens, the image of the

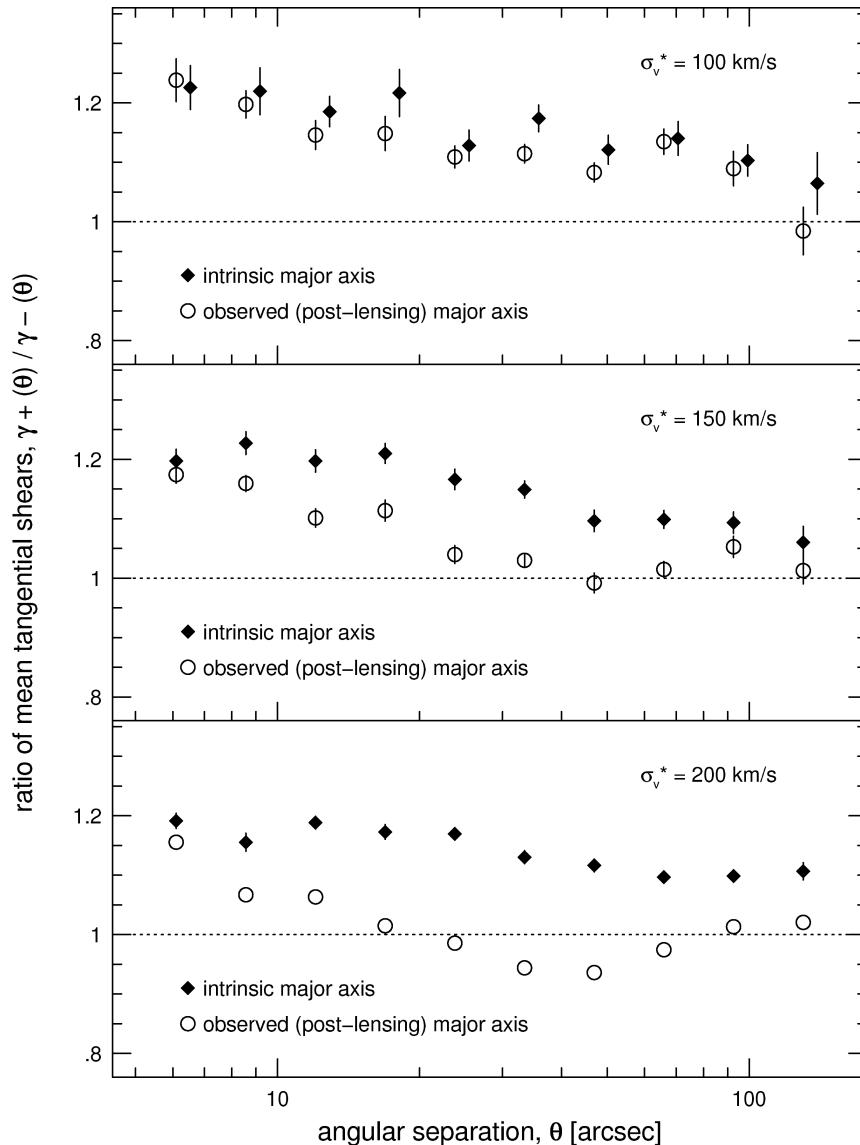


Figure 8. Ratio of the mean tangential shears, $\gamma^+(\theta)/\gamma^-(\theta)$, for three halo models adopted for the BTC40 galaxies. In all cases, the truncation radius of the haloes of L^* galaxies is taken to be $x_t^* = 100 h^{-1}$ kpc. Here all source galaxies that are located within $\pm 45^\circ$ of the symmetry axes of the bright, foreground centres are used in the calculation. Different point types indicate different definitions of the symmetry axes of the bright, foreground centres (circles: observed symmetry axes after lensing, diamonds: intrinsic symmetry axes). Error bars are omitted when they are comparable to or smaller than the data points. *Top:* $\sigma_v^* = 100 \text{ km s}^{-1}$. *Middle:* $\sigma_v^* = 150 \text{ km s}^{-1}$. *Bottom:* $\sigma_v^* = 200 \text{ km s}^{-1}$.

source galaxy is an ellipse with the major axis of its image oriented tangentially with respect to the major axis of the elliptical lens. This is illustrated by the blue ellipse in the top and bottom panels of Fig. 9. Now consider the effect on the image of the intrinsically circular source if a large mass (i.e. another galaxy) is placed in the foreground of the original lens–source pair. If the additional foreground mass is located along the line that connects the centroids of the original lens–source pair, the net result for the image of the intrinsically circular source is that it becomes *more elliptical* than if it had been lensed only once. This is illustrated by the red ellipse in the top panel of Fig. 9. Now consider the effect if the foreground mass is placed such that its location is tangential to the line that connects the centroids of the original lens–source pair. The net result for the image of the intrinsically circular source is that it will be *less elliptical* than if it had been lensed only once. This is illustrated by the red ellipse in the bottom panel of Fig. 9. We therefore see

that the inclusion of a second lens may either increase or decrease the net ellipticity of our distant, circular source over what we would have naively expected in the single-deflection case.

Next, let us consider the fact that not only will the introduction of an additional foreground mass alter the image of the distant, circular source galaxy, it will also alter the image of the original elliptical lens galaxy. Again, consider the original lens–source pair to be in the γ^+ configuration. If the foreground mass is placed along the line that connects the centroids of the original lens–source pair, the image of the elliptical lens becomes rounder than its intrinsic shape (i.e. since it is distorted tangentially with respect to the location of the foreground mass). In some finite number of cases where the intrinsic ellipticity of the image of the elliptical lens is very small and the shear due to the foreground lens is large, the post-lensing image of the elliptical lens may even have its observed symmetry axes reversed from its intrinsic symmetry axes. As a result, the

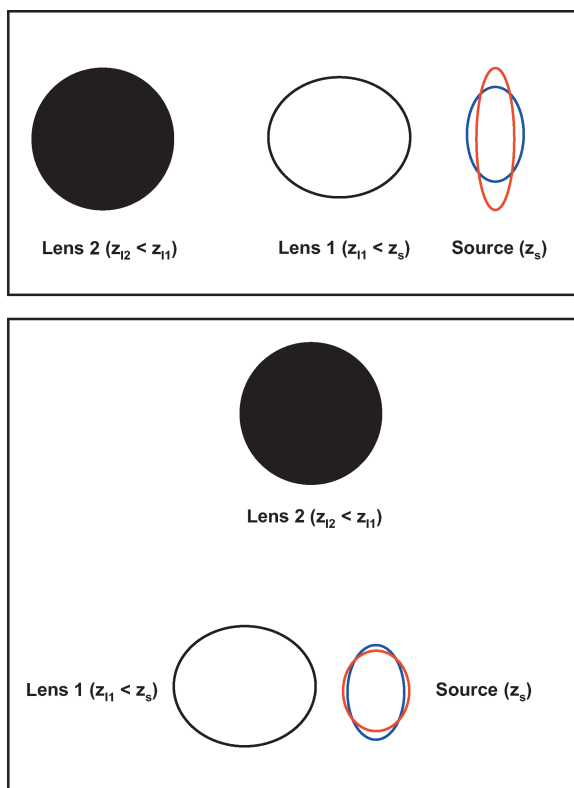


Figure 9. Schematic illustration of the net effect on the image of a distant, intrinsically circular source galaxy due to an elliptical lens with redshift $z_{l1} < z_s$ and an additional, foreground lens with redshift $z_{l2} < z_{l1}$. The black ellipse indicates the true shape and orientation of the elliptical lens. In both panels, the elliptical lens and the source are intrinsically in the ‘ γ^+ ’ configuration. Blue ellipses: shape of the source after lensing solely by the elliptical lens. Red ellipses: shape of the source after being lensed by the elliptical lens at z_{l1} and the additional foreground lens at z_{l2} . When the foreground lens is located along the direction vector that connects the centroids of the elliptical lens and the circular source, the final ellipticity of the image of the source is increased compared to what it would have been if the source had been lensed solely by the elliptical lens. When the foreground lens is located tangential to the direction vector that connects the centroids of the elliptical lens and the circular source, the final ellipticity of the image of the source is reduced compared to what it would have been if the source had been lensed solely by the elliptical lens. See the online version of this article for the colour figure.

distant, intrinsically circular source galaxy would appear to be in the γ^- configuration when, in fact, it is in the γ^+ configuration (e.g. top panel of Fig. 10). Should the situation illustrated in the top panel of Fig. 10 occur, the mean tangential shear that one would obtain for sources located close to the *observed minor axes* of the elliptical lens will be greater than it ought to be. That is, the observed value of γ^- is boosted by the incorrect inclusion of sources that would have properly gone into the calculation of γ^+ if one had known the orientation of the intrinsic symmetry axes of the elliptical lens. Of course, this also results in the observed value of γ^+ being reduced compared to its true value because the observed lens–source configuration has been ‘misclassified’ compared to its intrinsic configuration.

Next, consider placing the foreground mass along a line that is tangential to the line that connects the centroids of the original lens–source pair. If the original lens–source pair is in the γ^+ configuration, the image of the elliptical lens will have an increased ellipticity after being lensed by the foreground mass and it will not

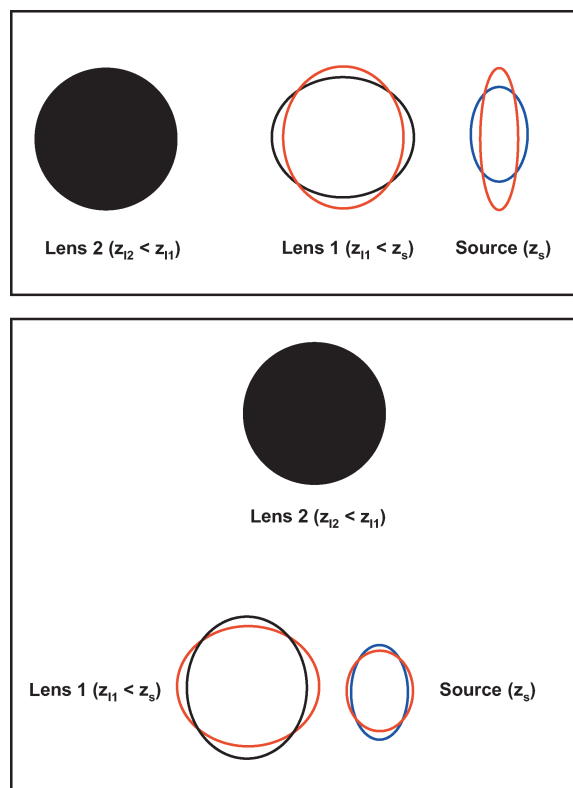


Figure 10. Schematic illustration of the net effect on (i) the image of a distant, intrinsically circular source galaxy due to an elliptical lens with redshift $z_{l1} < z_s$ and an additional, foreground lens with redshift $z_{l2} < z_{l1}$ and (ii) the image of the elliptical lens after being lensed by the foreground lens at z_{l2} . The black ellipse indicates the true shape and orientation of the elliptical lens and source are intrinsically in the ‘ γ^+ ’ configuration. Top: elliptical lens and source are intrinsically in the ‘ γ^+ ’ configuration. Bottom: elliptical lens and source are intrinsically in the ‘ γ^- ’ configuration. Blue ellipses: shape of the image of the source after lensing solely by the elliptical lens. Red ellipses: shape of the image of the elliptical lens after being lensed by the foreground lens at z_{l2} , as well as the shape of the image of the source after being lensed by the elliptical lens at z_{l1} and the additional foreground lens at z_{l2} . This figure illustrates that in the limit of small intrinsic ellipticities, the observed symmetry axes of the elliptical lens may be reversed from its intrinsic symmetry axes. This results in a misclassification of the configuration (γ^+ or γ^-) of the elliptical lens–source pair, which incorrectly enhances measurements of γ^- and incorrectly suppresses measurements of γ^+ . See the online version of this article for the colour figure.

undergo a reversal of its symmetry axes (i.e. the lens–source pair remains in the γ^+ configuration), but the final image of the source will be less elliptical than it would have been in the absence of the foreground lens. In the case that the lens–source pair is intrinsically in the γ^- configuration, however, a finite number of lenses with small intrinsic ellipticities may have their symmetry axes reversed by lensing due to the foreground mass (e.g. bottom panel of Fig. 10). Hence, the original lens–source pair would appear to be in the γ^+ configuration, when, in fact, it is actually in the γ^- configuration. In this case, the intrinsically circular source is incorrectly put into the calculation of γ^+ , and its net shear will be rather small because (i) it is, in reality, located near the minor axis of the elliptical lens and (ii) after being lensed by the additional foreground mass, its image will be rounder than if it had been lensed solely by the original elliptical lens. Both of these conspire to reduce the observed value of γ^+ compared to its true value.

Based upon relatively simple reasoning from Figs 9 and 10, we may therefore expect that multiple deflections (i.e. the presence of more than one foreground lens) could lead to a suppression of $\gamma^+(\theta)/\gamma^-(\theta)$ compared to what would be obtained if one knew the intrinsic symmetry axes of the bright centres. One might hope that in a sufficiently large data set, the effects of foreground lenses on the original elliptical lens–source pair would cancel each other out. However, this is not necessarily going to be the case. Galaxies span a broad range of redshifts; hence, at fixed angular separation from a source, θ , two foreground lens galaxies with identical gravitational potentials will have different lensing strengths because they are located at different physical distances from the source. In the following sections, we will explore the effect of galaxy–galaxy lensing on the images of the bright, foreground objects that are used as centres for the computation of the mean tangential shear of the faint, background objects. In addition, we will explore the effect of weak lensing of the central galaxies on the measured values of $\gamma^+(\theta)$ and $\gamma^-(\theta)$.

5 EFFECT OF GALAXY–GALAXY LENSING ON FOREGROUND GALAXY IMAGES

All of our Monte Carlo galaxies with redshifts z_i have been lensed by all other Monte Carlo galaxies with redshifts $z_j < z_i$ that are found within a radius of 100 arcsec of the galaxy at z_i . Since the redshift distribution of the galaxies is broad, this means that many of the bright centres (i.e. those BTC40 galaxies with $18 \leq I_{AB} \leq 20$) correspond to galaxies that have, themselves, been lensed (e.g. Fig. 4). At a given angular separation from a weak galaxy lens, galaxy–galaxy lensing may be considered to be a scalar shear. That is, although a source galaxy has a finite size on the sky, the shear due to a foreground weak galaxy lens is effectively constant across the image of the source. Shown in Fig. 11 is an illustration of the transformation of an ellipse (i.e. the intrinsic shape of a galaxy) due to a scalar shear. The important things to note from this figure are that a scalar shear applied to an ellipse results in a change in the ellipticity as

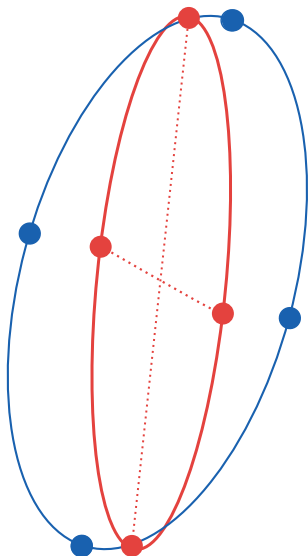


Figure 11. Transformation of an ellipse by a scalar shear. Blue: original ellipse. Red: transformed ellipse. Note that not only are the ellipticity and position angle of the ellipse altered, the original major and minor axes of the ellipse are no longer orthogonal. See the online version of this article for the colour figure.

well as a change in the position angle. In addition, the original major and minor axes of the ellipse are no longer orthogonal after the transformation.

In the limit that the intrinsic ellipticity, $\epsilon_{\text{in}} \equiv (a - b)/(a + b)$, of an ellipse is large compared to the applied shear, $\epsilon_{\text{in}} \gg \gamma/2$, the transformation of the ellipse due to a scalar shear can be obtained straightforwardly from equations (39) and (40) of Surpi & Harari (1999). Let the ellipse have intrinsic axial ratio $f = b/a$ and intrinsic position angle ψ . If we then take ϕ to be the angle between the major axis of the unlensed source ellipse and the vector that connects the centroids of the lens and the source ellipse, the resulting change in position angle of the source ellipse is

$$\Delta\psi \simeq \gamma \left(\frac{1 - f^2}{1 + f^2} \right) \sin 2(\phi - \psi) \quad (15)$$

and the square of the axial ratio of the transformed source ellipse is given by

$$(f')^2 = \frac{f^2 - 2\gamma f^2 \cos 2(\phi - \psi)}{1 + 2\gamma f^2 \cos 2(\phi - \psi)}. \quad (16)$$

Fig. 12 shows the resulting change in position angle and ellipticity for ellipses with intrinsic ellipticity $0.02 \leq \epsilon_{\text{in}} \leq 0.3$ due to a 1 per cent scalar shear ($\gamma = 0.01$). Unsurprisingly, the smaller is ϵ_{in} , the greater is the change in position angle, and the maximum change in the position angle occurs for $(\phi - \psi) = 45^\circ$. In addition, the smaller is ϵ_{in} , the greater is the change in ellipticity. The maximum change in ellipticity occurs for the two extreme conditions: $(\phi - \psi) \sim 0^\circ$, resulting in an ellipse that is rounder than its intrinsic shape, and $(\phi - \psi) \sim 90^\circ$, resulting in an ellipse that is flatter than its intrinsic shape.

6 EFFECT OF MULTIPLE WEAK DEFLECTIONS ON $\gamma^+(\theta)$ AND $\gamma^-(\theta)$

In the previous section we demonstrated that, in the limit of small intrinsic ellipticities, the images of the galaxies that correspond to the ‘bright centres’ in our galaxy–galaxy lensing analysis could be significantly affected by weak lensing by foreground galaxies under the right circumstances. That is, multiple weak deflections (in which a lens–source pair is subsequently lensed by one or more foreground galaxies) will affect not only the image of the original source, but they will also affect the image of the original lens. In this section, we investigate the effect of such multiple weak deflections on measurements of $\gamma^+(\theta)$ and $\gamma^-(\theta)$. Here, we wish to separate the effects of weak lensing due to non-spherical dark matter haloes from the effects of subsequent multiple weak deflections due to the haloes of foreground galaxies. To address this, we construct a set of constrained Monte Carlo simulations in which a lens–source pair that contains an elliptical lens is, itself, weakly lensed by additional galaxies whose dark matter haloes are spherically symmetric.

This second set of Monte Carlo simulations is constructed as follows. An elliptical lens of a fixed mass axial ratio, f , is placed at the origin of the coordinate system. Here, f is the axial ratio of the projected dark matter halo. The elliptical lens is assigned a random position angle and a redshift, z_{el} , drawn from the redshift distribution adopted for the BTC40 objects with apparent magnitudes $18 \leq I_{AB} \leq 20$. The elliptical lens is assigned an intrinsic, luminous galaxy shape drawn from equation (7), and the intrinsic position angle of the luminous lens galaxy is taken to be the position angle of its dark matter halo. A source galaxy is placed randomly along the horizontal axis of the coordinate system, such that it lies within a

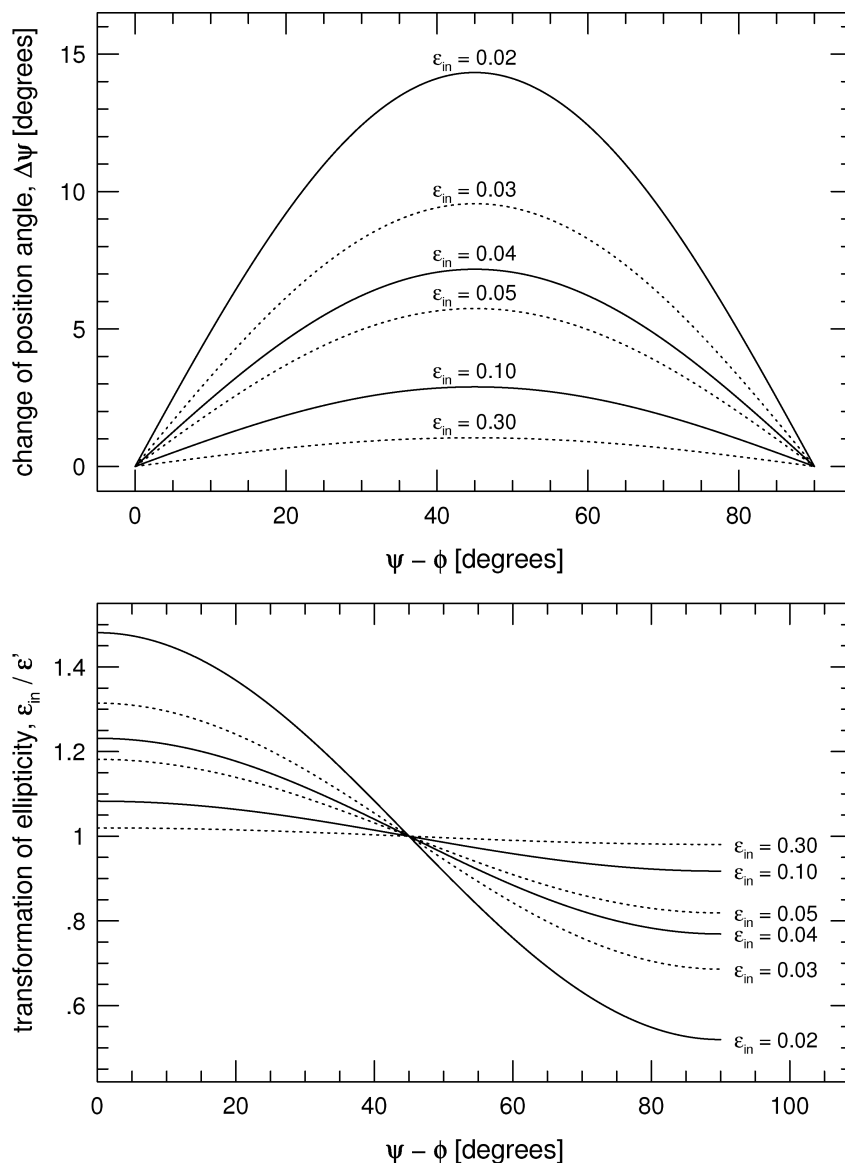


Figure 12. Transformation of an ellipse of intrinsic ellipticity, ϵ_{in} , due to a scalar shear of magnitude $\gamma = 0.01$. Prior to being sheared, the position angle of the ellipse is ψ . The quantity ϕ is the angle between the major axis of the unsheared source ellipse and the direction vector that connects the centroids of the lens and source. Top: change in the position angle of the ellipse. Bottom: ratio of intrinsic to transformed ellipticities.

distance of ± 30 arcsec of the elliptical lens. The source galaxy is assigned a fixed redshift, $z_s = 0.6$.

Next, a circle of a radius of 60 arcsec, centred on the elliptical lens, is populated with additional galaxy lenses whose haloes are taken to be singular isothermal spheres (SIS). The number density of the SIS lenses is matched to the observed number density of galaxies with apparent magnitudes $18 \leq I_{AB} \leq 20$ in the BTC40 data, and they are assigned random locations within the field. Each SIS lens is assigned a redshift based upon its apparent magnitude, again drawn from our adopted probability distribution.

The elliptical lens is assigned a velocity dispersion, σ_v , and truncation radius, x_t . For simplicity, the SIS lenses are assigned a velocity dispersion equal to the velocity dispersion that is assigned to the elliptical lens. Having assigned positions, redshifts and gravitational potentials to all of the lenses, then, the net shear experienced by the source is computed as the sum of the individual shears due

to all lenses (elliptical and SIS) with redshifts $z_l < 0.6$. In addition, the final image shape of the lens galaxy residing within the elliptical dark matter halo is computed using the net shear due to all foreground SIS lenses (i.e. SIS lenses with $z_l < z_{el}$).

The above procedure is repeated 20 million times for a fixed axial ratio, f , of the halo of the elliptical lens, fixed values of σ_v and x_t , and fixed source redshift $z_s = 0.6$. For each new Monte Carlo realization, a new intrinsic position angle and a new intrinsic image shape for the luminous galaxy within the elliptical lens halo are generated. That is, with each new realization, we randomly ‘spin’ the elliptical lens and assign its luminous galaxy a new intrinsic ellipticity. In addition, the elliptical lens is assigned a new redshift in each new realization. Thus, after many realizations, the redshifts of the elliptical lenses will span the entire range of redshift space that was adopted for BTC40 galaxies with $18 \leq I_{AB} \leq 20$. For each new Monte Carlo realization a new location for the source

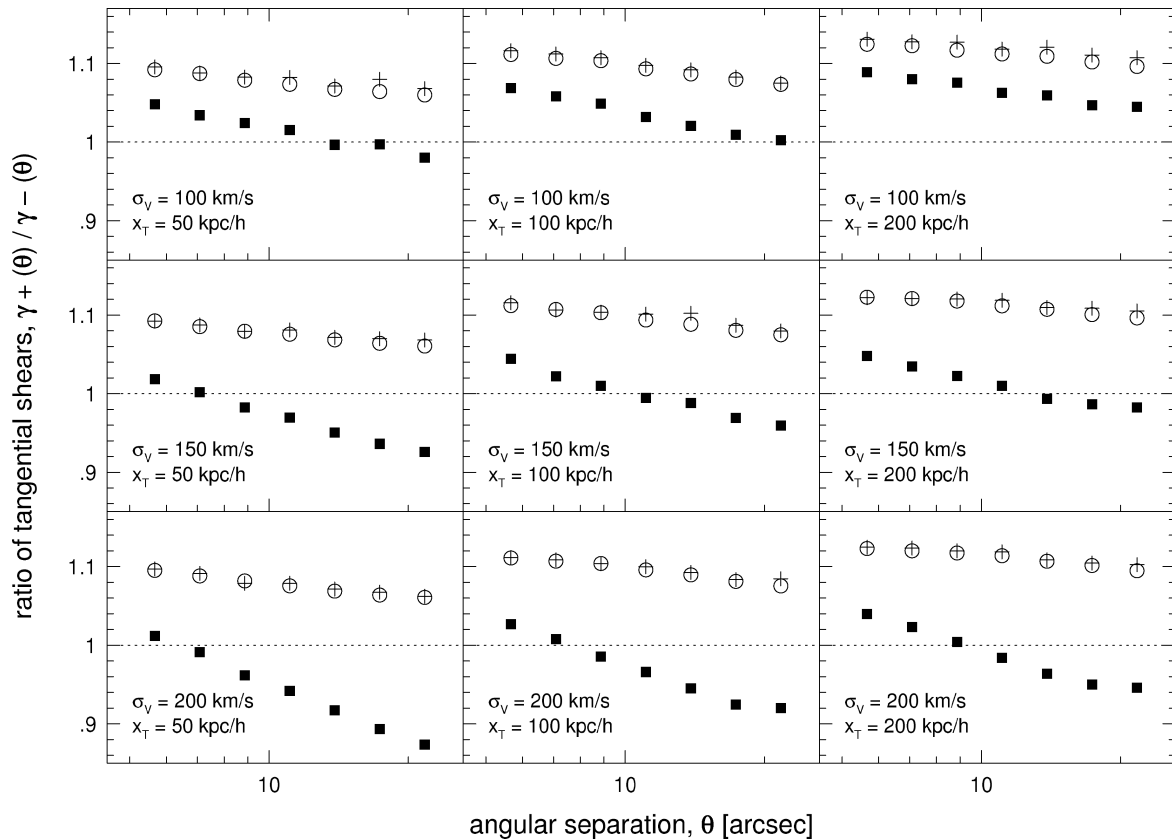


Figure 13. Ratio of mean tangential shears, $\gamma^+(\theta)/\gamma^-(\theta)$, for our suite of constrained Monte Carlo simulations. Here the halo of the central, elliptical lens galaxy has $\epsilon_{\text{halo}} = 0.1$. The function is measured relative to the symmetry axes of the central lens galaxy. Different panels show results for various values of the velocity dispersion and truncation radius of the central lens galaxy. All source galaxies located within $\pm 45^\circ$ of the symmetry axes of the central lens galaxy are included in the calculation. Error bars are omitted because they are comparable to or smaller than the data points. Circles: source galaxies have been lensed solely by the central, elliptical lens. Symmetry axes used in the calculation of $\gamma^+(\theta)/\gamma^-(\theta)$ are the intrinsic symmetry axes of the central lens. Crosses: source galaxies have been lensed by the central, elliptical lens as well as all foreground SIS lenses. Symmetry axes used in the calculation of $\gamma^+(\theta)/\gamma^-(\theta)$ are the intrinsic symmetry axes of the central lens. Squares: ‘observed’ signal. Source galaxies have been lensed by the central, elliptical lens as well as all foreground SIS lenses. The image of the central, elliptical lens has also been lensed by all foreground SIS lenses. Symmetry axes used in the calculation of $\gamma^+(\theta)/\gamma^-(\theta)$ are the final, observed symmetry axes of the central, elliptical lenses after lensing by the foreground SIS lenses.

along the horizontal axis is generated, and a new suite of SIS lenses is laid down (including new redshifts and new locations within the 60-arcsec circle). After the source at $z_s = 0.6$ and the elliptical lens at the origin have been lensed by all foreground galaxies, the net shear for both the source and the luminous galaxy within the elliptical halo are computed in each individual Monte Carlo realization. The mean tangential shear for the sources, γ^+ and γ^- , is then computed by taking the elliptical lenses as the centres for the calculation.

Shown in Figs 13–15 is the function $\gamma^+(\theta)/\gamma^-(\theta)$, obtained by computing the mean tangential shear for sources located within $\pm 45^\circ$ of the symmetry axes of the elliptical lens. Results from a range of halo parameters ($\sigma_v = 100, 150, 200 \text{ km s}^{-1}$; $x_t = 50, 100, 200 h^{-1} \text{ kpc}$) are shown in the different panels. Fig. 13 shows results for central elliptical lenses in which the ellipticity of the dark matter halo is $\epsilon_{\text{halo}} = 0.1$ (corresponding to a projected mass axial ratio $f = 0.82$). Fig. 14 shows results for central elliptical lenses in which the ellipticity of the dark matter halo is $\epsilon_{\text{halo}} = 0.3$ (corresponding to a projected mass axial ratio of $f = 0.54$). Fig. 15 shows results for central elliptical lenses in which the ellipticity of the dark matter halo is $\epsilon_{\text{halo}} = 0.5$ (corresponding to a projected mass axial ratio of $f = 0.33$).

The circles in Figs 13–15 show $\gamma^+(\theta)/\gamma^-(\theta)$ for the case that the source galaxies are lensed solely by the central elliptical lens. The

symmetry axes used for the calculation are the intrinsic symmetry axes of the central elliptical lens. In other words, the circles show the simplest expected result: all source galaxies are lensed by only one foreground galaxy, the lens has a non-spherical dark matter halo and the symmetry axes of the lens galaxy are its intrinsic symmetry axes. The crosses in Figs 13–15 show $\gamma^+(\theta)/\gamma^-(\theta)$ for the case that the source galaxies are lensed by both the central elliptical lens as well as all foreground SIS lenses. The symmetry axes used for the calculation are the intrinsic symmetry axes of the central elliptical lens. Comparing the crosses to the circles, we find that the introduction of foreground SIS lenses does little to affect the ratio of the tangential shears when the intrinsic symmetry axes of the central elliptical lens are used for the calculation.

The squares in Figs 13–15 show $\gamma^+(\theta)/\gamma^-(\theta)$ for the case that the source galaxies are lensed by both the central elliptical lens and all foreground SIS lenses. In addition, the central, elliptical lens has been lensed by all foreground SIS lenses. Here, the symmetry axes used for the calculation are the *observed* symmetry axes of the central elliptical lens (i.e. the symmetry axes after lensing by the foreground SIS lenses). From Figs 13–15, the degree to which the observed function, $\gamma^+(\theta)/\gamma^-(\theta)$, is suppressed compared to what one would obtain using the intrinsic symmetry axes of the elliptical lens is a function of the velocity dispersion that is adopted. The lower

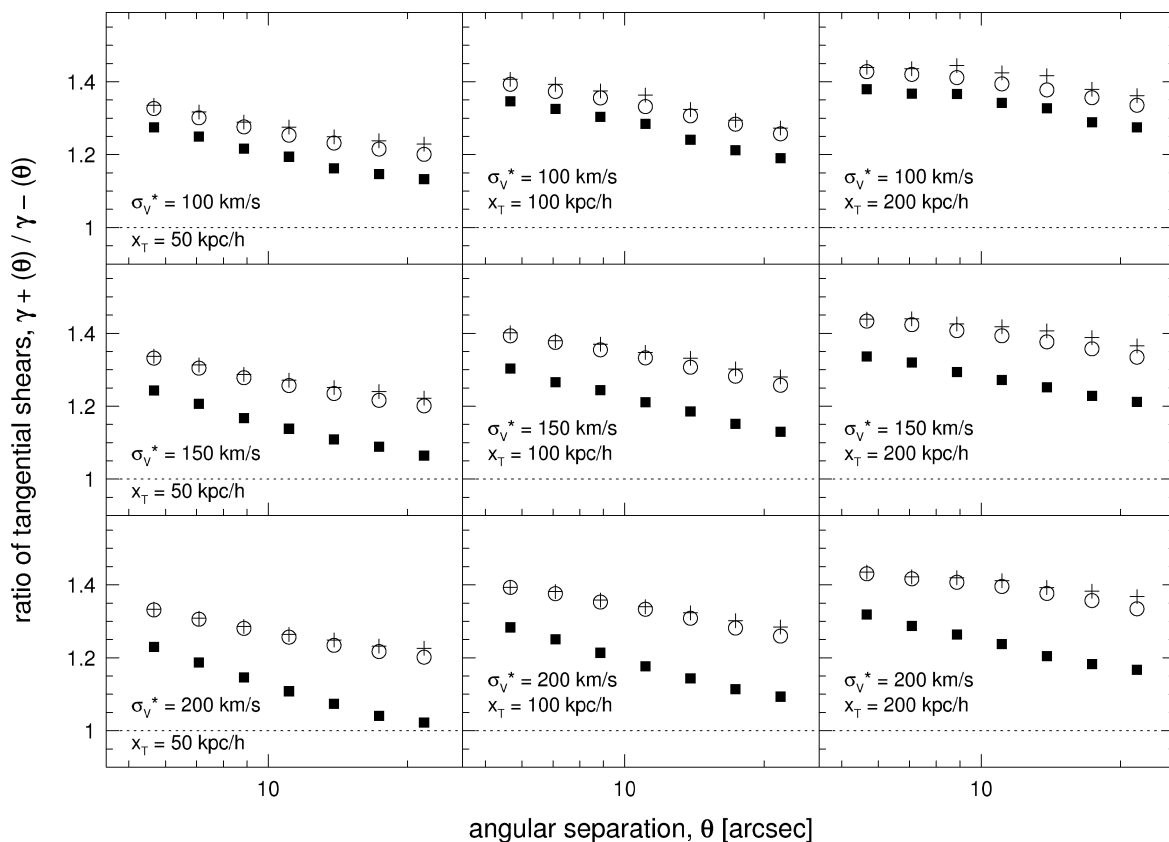


Figure 14. Same as Fig. 13 except that here the central, elliptical lens has $\epsilon_{\text{halo}} = 0.3$. Note that the vertical scale differs from that of Fig. 13.

is the velocity dispersion of the lenses, the less the observed function is suppressed. This is due to the fact that the frequency and strength of the multiple weak deflections are lower for lenses with low velocity dispersions than for lenses with high velocity dispersions (see e.g. Brainerd 2010). In contrast, the ellipticity of the projected dark matter halo of the central elliptical lens has relatively little effect on the degree to which the observed function, $\gamma^+(\theta)/\gamma^-(\theta)$, is suppressed. (Note that the vertical scales in Figs 13–15 are very different from each other due to the fact that the more elliptical is the central elliptical lens, the greater is the anisotropy that it induces.)

7 JUDICIOUS REJECTION OF LENSES AND SOURCES?

In an attempt to ‘inoculate’ one’s analysis of galaxy–galaxy lensing by non-spherical haloes against the above effects, one might consider simply rejecting bright centres with small image ellipticities from the calculation of $\gamma^+(\theta)$ and $\gamma^-(\theta)$. That is, one could hope to avoid the extreme situation where a lens–source pair that is truly in the ‘ γ^+ ’ configuration is swapped to the ‘ γ^- ’ configuration due to the ellipticity of the image of the lens being very small (and, hence, making it more susceptible to having its symmetry axes altered significantly by weak lensing due to foreground galaxies). Naively, one might hope that the suppression of the observed function, $\gamma^+(\theta)/\gamma^-(\theta)$, could be eliminated simply by choosing to compute the mean tangential shear using bright centres whose images are highly elliptical.

In addition, in a search for the signature of anisotropic galaxy–galaxy lensing, one might be tempted to restrict the analysis to

source galaxies that are very close to the symmetry axes of the bright centres that are used to calculate the mean tangential shear. That is, in all of the above analyses, $\gamma^+(\theta)$ and $\gamma^-(\theta)$ were computed using all sources whose azimuthal coordinates, φ , placed them within $\pm 45^\circ$ of the symmetry axes of the bright centres. At fixed angular separation from an elliptical lens, the maximal difference in the shear experienced by two sources will, of course, occur when one source is located along the minor axis of the lens and the other is located along the major axis of the lens. Therefore, one might expect that if one narrowed the analysis region from $\pm 45^\circ$ to, say, $\pm 25^\circ$ or $\pm 15^\circ$, it would be easier to detect anisotropic galaxy–galaxy lensing.

Unfortunately, the situation is not that simple in either of these cases. Weak lensing of the bright centres may make their resulting images either rounder or more elliptical than their intrinsic image shape (i.e. bottom panel of Fig. 12). Suppose that one chooses a minimum image ellipticity for the bright centres and that the computation of $\gamma^+(\theta)$ and $\gamma^-(\theta)$ is performed using only those bright centres with observed ellipticity $\epsilon_{\text{light}} > \epsilon_{\text{cut}}$. Some fraction of the bright centres whose intrinsic ellipticity truly exceeds ϵ_{cut} will, by weak lensing by foreground galaxies, have their resulting images made rounder than their intrinsic ellipticity. As a result, some bright centres with intrinsic ellipticities that are larger than ϵ_{cut} will, in fact, be rejected on because their observed (post-lensing) images have ellipticities smaller than ϵ_{cut} . The number of such bright centres that are affected by this will vary with the magnitude of the shear that they experience.

In addition to changing the ellipticity, weak lensing of the bright centres may rotate the orientations of their symmetry axes (i.e. top panel of Fig. 12). If one simply tries to narrow one’s analysis region

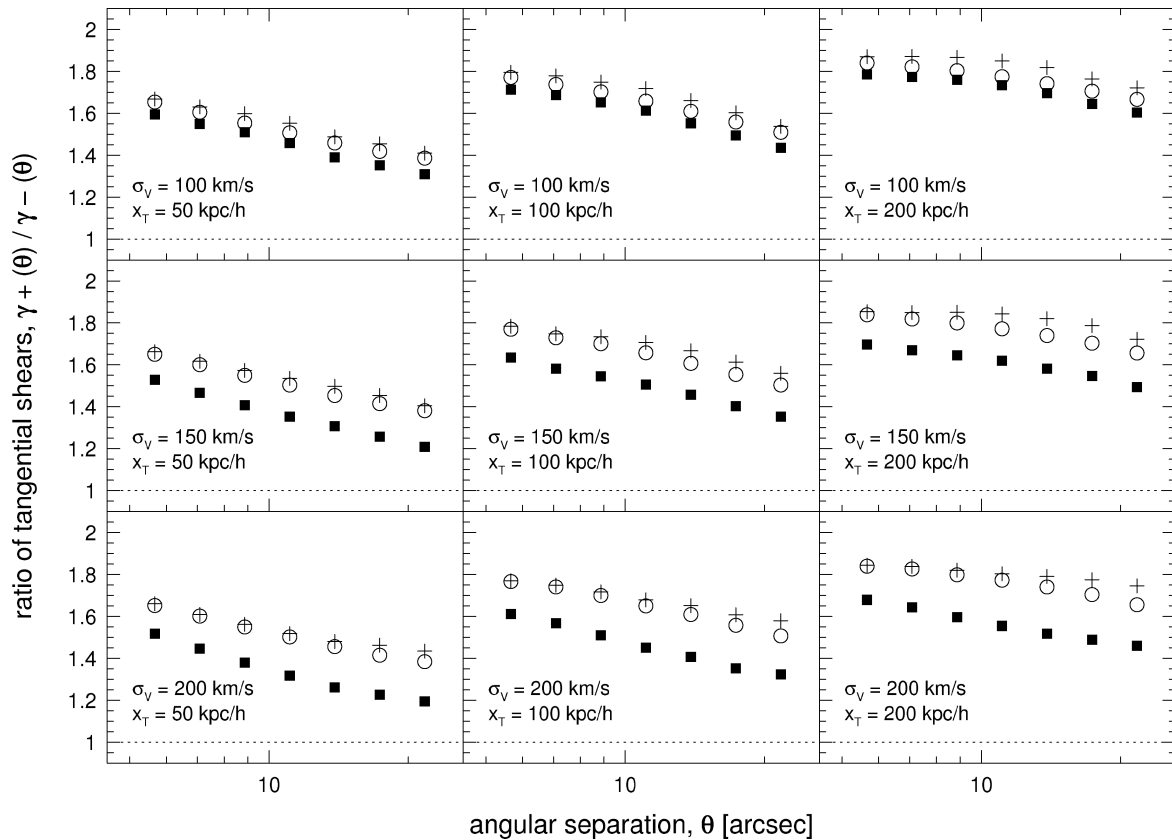


Figure 15. Same as Fig. 13 except that here the central, elliptical lens has $\epsilon_{\text{halo}} = 0.5$. Note that the vertical scale differs from that of Fig. 13.

relative to the symmetry axes of the bright centres, a problem will occur if the bright centres have been weakly lensed. Any rotation of the symmetry axes of the bright centres causes the analysis region that one truly desires (i.e. the region that brackets the directions of the major and minor axes of the projected halo mass) to be rotated with respect to the analysis region that one must actually use in practice (i.e. the region that brackets the directions of the observed major and minor axes of the image of the bright centre). Therefore, narrowing the analysis region may actually increase the discrepancy between the observed function, $\gamma^+(\theta)/\gamma^-(\theta)$, and the function that one would measure if the intrinsic symmetry axes of the bright centres were known.

In this section we adopt a fiducial elliptical lens with velocity dispersion $\sigma_v = 150 \text{ km s}^{-1}$, truncation radius $x_t = 100 h^{-1} \text{ kpc}$ and projected halo ellipticity $\epsilon = 0.3$, and we construct Monte Carlo simulations that are identical to the Monte Carlo simulations in Section 6 (i.e. the simulations used to obtain the central panel of Fig. 14). Shown in Fig. 16 is the effect of narrowing the analysis region when computing the ratio of the mean tangential shears. The left-hand panel of Fig. 16 shows the observed and intrinsic functions, $\gamma^+(\theta)/\gamma^-(\theta)$, when all sources within $\pm 45^\circ$ of the symmetry axes of the central, elliptical lens are used for the calculations. The right-hand panel of Fig. 16 shows the same functions as the left-hand panel, but here only sources that are within $\pm 15^\circ$ of the symmetry axes of the central, elliptical lens are used for the calculations. From the right-hand panel of Fig. 16, it is clear that narrowing the analysis region (i.e. using only sources that are very close to the symmetry axes) increases the degree of anisotropy in the galaxy–galaxy lensing signal. However, narrowing the analysis region also increases the disparity between the observed function, $\gamma^+(\theta)/\gamma^-(\theta)$, and the

function that would be measured if the intrinsic symmetry axes of the central, elliptical lenses were known.

Fig. 17 shows the effect of rejecting bright centres whose images (post-lensing) are very round. All sources within $\pm 45^\circ$ of the symmetry axes of the central, elliptical lens are used in the calculation. Here circles show the observed function, $\gamma^+(\theta)/\gamma^-(\theta)$, and crosses show the function that one would obtain if the intrinsic symmetry axes of the central elliptical lens were known. In the case of the circles and crosses, no constraint on the ellipticity of the lens image is imposed. Triangles in Fig. 17 show the observed function, $\gamma^+(\theta)/\gamma^-(\theta)$, where the ratio has been computed using the observed symmetry axes of central, elliptical galaxies whose images (post-lensing) have ellipticities $\epsilon_{\text{light}} > 0.3$. From this figure, then, rejection of lenses with image ellipticities $\epsilon_{\text{light}} < 0.3$ increases the observed function, $\gamma^+(\theta)/\gamma^-(\theta)$, only slightly. In particular, rejection of the lenses with the roundest images does not allow one to recover the function that one would measure if the intrinsic symmetry axes of the central, elliptical lenses were known.

8 SUMMARY AND CONCLUSIONS

We have investigated the theory of galaxy–galaxy lensing by non-spherical dark matter haloes, which should give rise to an anisotropy in the tangential shear experienced by distant source galaxies. If each distant source is lensed by only one foreground elliptical lens, and if the observed symmetry axes of the elliptical lens correspond to the intrinsic symmetry axes of its projected dark matter halo, one would expect the signature of anisotropic galaxy–galaxy lensing to manifest as $\gamma^+(\theta) > \gamma^-(\theta)$ over a wide range of angular scales. Here, $\gamma^+(\theta)$ is the angular dependence of the mean tangential shear

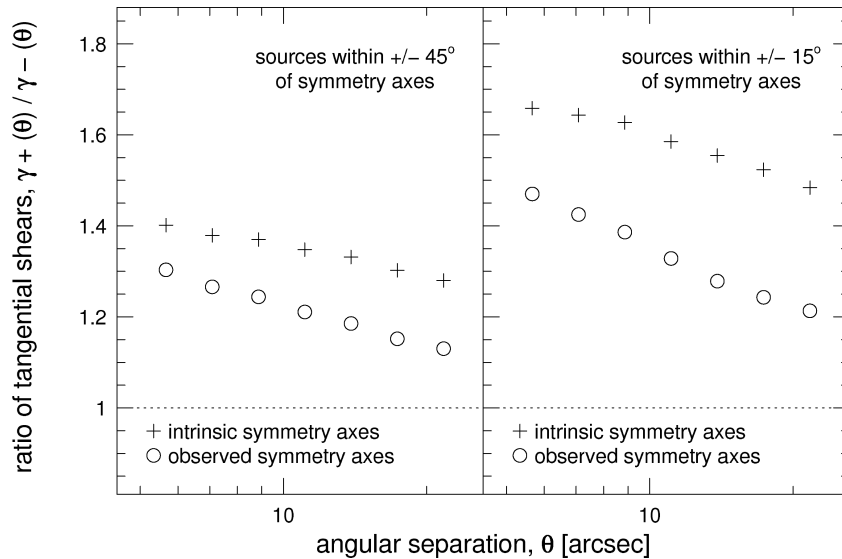


Figure 16. Effect of narrowing the analysis region on the ratio of mean tangential shears. Here a fiducial elliptical lens with $\sigma_v = 150 \text{ km s}^{-1}$, $x_t = 100 h^{-1} \text{ kpc}$ and projected halo ellipticity $\epsilon_{\text{halo}} = 0.3$ has been adopted. Circles: ‘observed’ signal. Sources have been lensed by the central, elliptical lens and all foreground SIS lenses. The central, elliptical lens has also been lensed by all foreground SIS lenses and its observed symmetry axes are used for the calculation. Crosses: sources have been lensed by the central, elliptical lens and all foreground SIS lenses. The intrinsic (unlensed) symmetry axes of the central lens are used for the calculation. *Left:* all sources within $\pm 45^\circ$ of the lens symmetry axes are used in the calculations. *Right:* only sources within $\pm 15^\circ$ of the lens symmetry axes are used in the calculations. Narrowing the analysis region increases the degree of anisotropy in the galaxy–galaxy lensing signal, but it also increases the disparity between the observed signal and the one that would be measured if the intrinsic symmetry axes of the lenses were known.

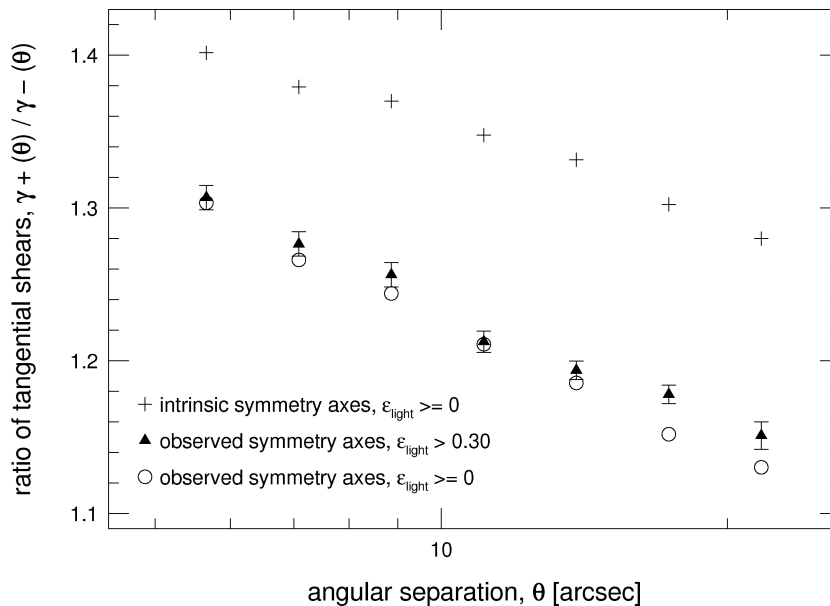


Figure 17. Effect of rejection of round lenses on the ratio of the mean tangential shears. Here all sources within $\pm 45^\circ$ of the symmetry axes of the central, elliptical lens are used. The central, elliptical lens has halo parameters $\sigma_v = 150 \text{ km s}^{-1}$, $x_t = 100 h^{-1} \text{ kpc}$ and projected ellipticity $\epsilon_{\text{halo}} = 0.3$. Error bars are omitted when they are comparable to or smaller than the data points. Circles: ‘observed’ signal. Sources have been lensed by the central, elliptical lens and all foreground SIS lenses. The central, elliptical lens has also been lensed by all foreground SIS lenses and its observed symmetry axes are used for the calculation. No constraint has been placed on the ellipticity of the image of the central, elliptical galaxy. Crosses: sources have been lensed by the central, elliptical lens and all foreground SIS lenses. The intrinsic (unlensed) symmetry axes of the central lens are used for the calculation. No constraint has been placed on the ellipticity of the image of the central, elliptical galaxy. Triangles: ‘observed’ signal, computed using only those central, elliptical lenses whose observed (post-lensing) image ellipticity is $\epsilon_{\text{light}} > 0.3$. Rejection of central, elliptical galaxies with very round images does little to affect the discrepancy between the observed function and the one that would be obtained if the intrinsic symmetry axes of the central, elliptical lenses were known.

experienced by sources whose azimuthal coordinates place them close to the major axis of the lens and $\gamma^-(\theta)$ is the angular dependence of the mean tangential shear experienced by sources whose azimuthal coordinates place them close to the minor axis of the lens.

Using an observational data set (observed coordinates and I -band apparent magnitudes) as a framework for a set of Monte Carlo simulations, we have demonstrated that the actual signature that one should expect to observe for anisotropic galaxy–galaxy lensing is

far from the above idealized case. Because galaxies are broadly distributed in redshift space, it is common for a distant source galaxy located at redshift z_s to be lensed by another galaxy located at redshift $z_{l1} < z_s$. In turn, this original lens–source pair may then be lensed by yet another galaxy (or galaxies) located at redshift $z_{l2} < z_{l1}$. Such instances of ‘multiple deflections’ cause the observed signature of anisotropic galaxy–galaxy lensing to deviate from the expected signature. The degree to which the observed signature of galaxy–galaxy lensing deviates from the expected signature is a strong function of the characteristic velocity dispersion of the haloes of L^* galaxies. In the case of low characteristic velocity dispersions, $\sigma_v^* = 100 \text{ km s}^{-1}$, the observed ratio of mean tangential shears, $\gamma^+(\theta)/\gamma^-(\theta)$, exceeds a value of unity on all scales $\theta < 100$ arcsec and is only slightly lower than the function one would obtain if the intrinsic symmetry axes of the foreground galaxies were used to perform the calculation. In the case of moderate velocity dispersions, $\sigma_v^* = 150 \text{ km s}^{-1}$, the observed ratio of mean tangential shears shows little to no anisotropy on scales $\theta > 20$ arcsec. In the case of high velocity dispersions, $\sigma_v^* = 200 \text{ km s}^{-1}$, the observed function is actually reversed from the expected function [i.e. $\gamma^+(\theta) < \gamma^-(\theta)$] on scales $20 \text{ arcsec} < \theta < 70 \text{ arcsec}$ and is consistent with no anisotropy on scales $70 \text{ arcsec} < \theta < 120 \text{ arcsec}$.

In summary, our simulations show that if one observes $\gamma^+(\theta) = \gamma^-(\theta)$ in a large galaxy–galaxy lensing data set, the observation cannot be simply interpreted as proof that the haloes of the lens galaxies are spherically symmetric. That is, although the measured signal appears to be isotropic, it is entirely possible that anisotropic galaxy–galaxy lensing by non-spherical haloes may have taken place. Further, our simulations show that if one observes $\gamma^+(\theta) < \gamma^-(\theta)$ in a large galaxy–galaxy lensing data set, the observation cannot be simply interpreted as proof that mass and light are ‘anti-aligned’ in the lens galaxies. That is, although the measured signal appears to be reversed from the expected signal, the reversal may occur when mass and light are, in fact, perfectly aligned within the lens galaxies.

The primary reason that the observed signature of anisotropic galaxy–galaxy lensing differs from the expected signature is that the foreground galaxies that are used as centres to compute the mean tangential shear have, themselves, been weakly lensed. The expectation that $\gamma^+(\theta)$ will exceed $\gamma^-(\theta)$ over a wide range of angular scales is based upon a picture in which the observed symmetry axes of the lenses are identical to the intrinsic symmetry axes of their projected dark matter haloes. However, when one computes $\gamma^+(\theta)$ and $\gamma^-(\theta)$ in an observational data set, one cannot directly view the intrinsic symmetry axes of the bright, central galaxies. Instead, one is forced to use their observed symmetry axes and, in general, these will differ from the intrinsic symmetry axes.

Our simulations show that, even in the limit of multiple deflections being experienced by the distant source galaxies, if one could use the intrinsic symmetry axes of the lenses to define the geometry of the problem, one would expect to observe $\gamma^+(\theta) > \gamma^-(\theta)$. That is, multiple deflections experienced by the source galaxies have little effect on the intrinsic signature of anisotropic galaxy–galaxy lensing by non-spherical haloes. However, weak lensing of the bright, central foreground galaxies causes their observed symmetry axes [which are used to define the geometry for the calculation of $\gamma^+(\theta)$ and $\gamma^-(\theta)$] to differ from their intrinsic symmetry axes (i.e. the unlensed symmetry axes, which define the geometry for the actual lensing of the distant galaxies). It is this change in the symmetry axes of the bright, foreground galaxies that gives rise to the suppression of the observed function, $\gamma^+(\theta)/\gamma^-(\theta)$, compared to the function that would be obtained if the intrinsic symmetry axes were used for the calculation. The effects of weak lensing of the bright,

foreground galaxies on an observation of $\gamma^+(\theta)/\gamma^-(\theta)$ cannot be eliminated simply by rejecting foreground galaxies with very small image ellipticities or by using sources that are particularly close to the observed symmetry axes of the foreground galaxies.

We conclude therefore that in order to properly interpret any observed galaxy–galaxy lensing signal (be it isotropic or anisotropic), it is vital that full, multiple-deflection Monte Carlo simulations be used. Especially important is accounting for the fact that the images of the bright, foreground centres are likely to have been weakly lensed. If the effects of multiple deflections are not taken into account when interpreting an observed galaxy–galaxy lensing signal, there is a high probability that incorrect conclusions will be drawn about the nature of the haloes surrounding the lens galaxies.

ACKNOWLEDGMENTS

It is a pleasure to thank the BTC40 survey team, particularly Emilio Falco, Chris Kochanek, Malcolm Smith and Richard Green, for allowing us to use their data. Support from the National Science Foundation under NSF contracts AST-0406844 and AST-0708468 is gratefully acknowledged.

REFERENCES

- Abazajian K. et al., 2009, *ApJS*, 182, 543
 Agustsson I., Brainerd T. G., 2006, *ApJ*, 650, 500
 Allgood B., Flores R. A., Primack J. R., Kravtsov A. V., Wechsler R. H., Faltenbacher A., Bullock J. S., 2006, *MNRAS*, 367, 1781
 Bailin J., Steinmetz M., 2005, *ApJ*, 627, 647
 Bartelmann M., Schneider P., 2001, *Phys. Rep.*, 340, 297
 Bertin E., Arnouts S., 1996, *A&AS*, 117, 393
 Brainerd T. G., 2010, *ApJ*, 713, 603
 Brainerd T. G., Blandford R. D., 2002, in Courbin, F., Minniti, D., eds, *Lecture Notes in Physics Vol. 608, Gravitational Lensing: An Astrophysical Tool*. Springer, Berlin, p. 96
 Brainerd T. G., Blandford R. D., Smail I., 1996, *ApJ*, 466, 623 (BBS)
 Cohen J., Hogg D. W., Pahre M. A., Blandford R., Shopbell P. L., 1999a, *ApJ*, 512, 30
 Cohen J., Hogg D. W., Blandford R., Shopbell P. L., Richberg K., 1999b, *ApJS*, 120, 171
 Ebbels T., 1998, PhD thesis, Univ. of Cambridge
 Evans A. K., Bridle S., 2009, *MNRAS*, 695, 1446
 Fischer P. et al., 2000, *AJ*, 120, 1198
 Guzik J., Seljak U., 2002, *MNRAS*, 335, 311
 Heymans C. et al., 2006, *MNRAS*, 371, L60
 Hoekstra H., Yee H. K. C., Gladders M. D., 2004, *ApJ*, 606, 67
 Hoekstra H., Hsieh B. C., Yee H. K. C., Lin H., Gladders M. D., 2005, *ApJ*, 653, 73
 Jing Y. P., Suto Y., 2002, *ApJ*, 574, 538
 Kasun S. F., Evrard A. E., 2005, *ApJ*, 629, 781
 Kleinheinrich M. et al., 2006, *AA*, 455, 441
 Kormann R., Schneider P., Bartelmann M., 1994, *AA*, 284, 285
 LeFèvre O., Hudon D., Lilly S. J., Crampton D., Hammer F., Tresse L., 1996, *ApJ*, 461, 534
 LeFèvre O. et al., 2004, *A&A*, 428, 1043
 Limousin M., Kneib J.-P., Bardeau S., Natarajan P., Czoske O., Smail I., Ebling H., Smith G. P., 2007, *A&A*, 461, 881
 Mandelbaum R., Seljak U., Kauffmann G., Hirata C. M., Brinkmann J., 2006a, *MNRAS*, 368, 715
 Mandelbaum R., Hirata C. M., Broderick T., Seljak U., Brinkmann J., 2006b, *MNRAS*, 370, 1008
 Mandelbaum R., Seljak U., Hirata C. M., 2008, *J. Cosmol. Astropart. Phys.*, 8, 6
 Monier E. M., Kenefick J. D., Hall P. B., Osmer P. S., Smith M. G., Dalton G. B., Green R. F., 2002, *AJ*, 124, 2971

- Natarajan P., Kneib J.-P., Smail I., Treu T., Ellis R., Moran S., Limousin M., Czoske O., 2009, *ApJ*, 693, 970
- Navarro J. F., Frenk C. S., White S. D. M., 1995, *MNRAS*, 275, 720
- Navarro J. F., Frenk C. S., White S. D. M., 1996, *ApJ*, 462, 563
- Navarro J. F., Frenk C. S., White S. D. M., 1997, *ApJ*, 490, 493
- Parker L. C., Hoekstra H., Hudson M. J., van Waerbeke L., Mellier Y., 2007, *ApJ*, 669, 21
- Sheldon E. et al., 2004, *AJ*, 127, 2544
- Surpi G. C., Harari D. D., 1999, *ApJ*, 515, 455
- Tian L., Hoekstra H., Zhao H., 2009, *MNRAS*, 393, 885
- Tyson J. A., Bernstein G. M., Blouke M. M., Lee R. W., 1992, in Blouke M. M., Chang W., Thorpe L. J., Khosla R. P., eds, *Proc. SPIE 1656, A Large Area CCD Mosaic for Astronomy*. SPIE, Bellingham, p. 400
- Warren M. S., Quinn P. J., Salmon J. K., Zurek W. H., 1992, *ApJ*, 399, 405
- Wittman D. M., Tyson J. A., Bernstein G. M., Lee R. W., Dell’Antonio I. P., Fischer P., Smith D. R., Blouke M. M., 1998, in D’Odorico S., ed., *Proc. SPIE 3355, Optical Astronomical Instrumentation*. SPIE, Bellingham, p. 626
- Wright C. O., 2002, PhD thesis, Boston Univ.

This paper has been typeset from a $\text{\TeX}/\text{\LaTeX}$ file prepared by the author.